

## Atmospheric component of the MPI-M Earth System Model: ECHAM6

Bjorn Stevens,<sup>1</sup> Marco Giorgetta,<sup>1</sup> Monika Esch,<sup>1</sup> Thorsten Mauritsen,<sup>1</sup> Traute Crueger,<sup>1</sup> Sebastian Rast,<sup>1</sup> Marc Salzmann,<sup>1,2</sup> Hauke Schmidt,<sup>1</sup> Jürgen Bader,<sup>1</sup> Karoline Block,<sup>1</sup> Renate Brokopf,<sup>1</sup> Irina Fast,<sup>3</sup> Stefan Kinne,<sup>1</sup> Luis Kornbluh,<sup>1</sup> Ulrike Lohmann,<sup>4</sup> Robert Pincus,<sup>5</sup> Thomas Reichler,<sup>6</sup> and Erich Roeckner<sup>1</sup>

Received 29 July 2012; revised 21 December 2012; accepted 4 January 2013; published 18 April 2013.

[1] ECHAM6, the sixth generation of the atmospheric general circulation model ECHAM, is described. Major changes with respect to its predecessor affect the representation of shortwave radiative transfer, the height of the model top. Minor changes have been made to model tuning and convective triggering. Several model configurations, differing in horizontal and vertical resolution, are compared. As horizontal resolution is increased beyond T63, the simulated climate improves but changes are incremental; major biases appear to be limited by the parameterization of small-scale physical processes, such as clouds and convection. Higher vertical resolution in the middle atmosphere leads to a systematic reduction in temperature biases in the upper troposphere, and a better representation of the middle atmosphere and its modes of variability. ECHAM6 represents the present climate as well as, or better than, its predecessor. The most marked improvements are evident in the circulation of the extratropics. ECHAM6 continues to have a good representation of tropical variability. A number of biases, however, remain. These include a poor representation of low-level clouds, systematic shifts in major precipitation features, biases in the partitioning of precipitation between land and sea (particularly in the tropics), and midlatitude jets that appear to be insufficiently poleward. The response of ECHAM6 to increasing concentrations of greenhouse gases is similar to that of ECHAM5. The equilibrium climate sensitivity of the mixed-resolution (T63L95) configuration is between 2.9 and 3.4 K and is somewhat larger for the 47 level model. Cloud feedbacks and adjustments contribute positively to warming from increasing greenhouse gases.

**Citation:** Stevens, B., et al. (2013), Atmospheric component of the MPI-M Earth System Model: ECHAM6, *J. Adv. Model. Earth Syst.*, 5, 146–172, doi:10.1002/jame.20015.

### 1 Introduction

[2] ECHAM6 is the sixth generation of the atmospheric general circulation model ECHAM, developed by the Max Planck Institute for Meteorology (MPI-M)

in Hamburg, Germany. The original ECHAM model branched from an early release of the European Center (EC) for Medium Range Weather Forecasts (ECMWF) model to climate studies [Roeckner *et al.*, 1989]. Hence its name, ECHAM, which fuses the EC from ECMWF and HAM for Hamburg. Since its inception, ECHAM has served as the atmospheric component of a coupled modeling system. The present version of the coupled system, the MPI Earth System Model (or MPI-ESM) is described in an accompanying paper (M. Giorgetta *et al.*, Climate change from 1850 to 2100 in MPI-ESM: simulations for the Coupled Model Intercomparison Project, Phase 5, submitted to *Journal of Advances in Modeling Earth Systems*, 2012, hereinafter referred to as Giorgetta *et al.*, submitted manuscript, 2012). ECHAM6, the MPI-ESM, and all of their predecessors have been developed by scientists at the MPI-M over the past 25 years for the purpose of understanding Earth's changing climate.

<sup>1</sup>Max Planck Institute for Meteorology, KlimaCampus, Hamburg, Germany.

<sup>2</sup>Now at University of Leipzig, Institute for Meteorology, Leipzig, Germany.

<sup>3</sup>German Climate Computing Center (DKRZ), KlimaCampus, Hamburg, Germany.

<sup>4</sup>Institute for Atmospheric and Climate Science, ETH Zurich, Zurich, Switzerland.

<sup>5</sup>University of Colorado and NOAA Earth System Research Lab, Physical Sciences Division, Boulder, Colorado, USA.

<sup>6</sup>Department of Meteorology, University of Utah, Salt Lake City, Utah, USA.

[3] In the past ECHAM has been extensively documented through internal reports, rather than in the refereed literature. Often referred to as the gray literature, these reports do not have the archival character of the refereed literature. Given changes in electronic publishing, such reports are becoming increasingly less accessible, and less acceptable, all the more so with the rise of coordinated projects such as the coupled model inter-comparison project (presently phase 5, or CMIP5, Taylor *et al.* [2012]), for which model output is widely used by those not active in the model development. The primary motivation of this paper is thus to document, in the open literature, ECHAM6. A secondary motivation is, given the long history of model development at the MPI-M, to assess the present status of ECHAM in the context of over a quarter century of development. How has our ability to simulate the atmospheric component of the climate system advanced? Which types of model developments have been emphasized? How has model resolution evolved in comparison to other facets of the model? As many of the original developers of ECHAM are beginning to retire, such a retrospective is opportune.

[4] The remainder of this manuscript is organized as follows. A brief overview of changes made to ECHAM6 in the context of the past development of ECHAM is presented in section 2. A more detailed description of the model is presented in section 3. Section 3 is more extensive than it would have been, had previous versions of ECHAM been adequately described in the open literature. In section 4, the capability of ECHAM6 to represent the present climate is explored in comparison to previous generations of ECHAM and as a function of model resolution. The climate sensitivity of ECHAM6, and basic properties of its response to changing concentrations of greenhouse gases, are documented in section 5. Section 6 concludes the manuscript with a summary.

## 2. A Brief Historical Overview of ECHAM

[5] In this section, changes introduced in ECHAM6 are placed in the context of the overall ECHAM development. These changes involve modifications to its core physical content, with most emphasis being on the parameterization of diabatic processes, changes in the models and submodels to which ECHAM has been coupled, and the native resolution over which it has been run.

[6] ECHAM1 [Roeckner *et al.*, 1989] differed from its parent atmospheric model, the cycle 17 model operational at the ECMWF in 1985 [Simmons *et al.*, 1989], primarily through changes in, or the addition of, diabatic processes; for instance, a revised treatment of radiative transfer, a prognostic treatment of the stratiform clouds, and a shallow convection were introduced. ECHAM2 was a little-used version of ECHAM, which differed only nominally from ECHAM1 through its treatment of surface orography and ocean coupling [Lunkeit *et al.*, 1996]. ECHAM3 incorporated more major changes, including the development of a compre-

hensive mass flux scheme for the representation of cumulus convection, the generalization of the planetary boundary layer model to include moist processes, and improved representation of tracer transport [Roeckner *et al.*, 1992]. ECHAM4, released in 1996, incorporated changes to many of the physical parameterizations, including the representation of deep cumulus convection, land-surface parameters, and tracer transport [Roeckner *et al.*, 1996]. ECHAM5, released in 2003 [Roeckner *et al.*, 2003], included new representations of tracer transport and longwave radiation, and began a major overhaul of the representation of land-surface processes, which remains on going [Raddatz *et al.*, 2007; Brovkin *et al.*, 2009] (C. Reick *et al.*, The representation of natural and anthropogenic land cover change in MPI-ESM, submitted to *Journal of Advances in Modeling Earth Systems*, 2012). In addition to the ongoing work on the land surface, changes introduced in ECHAM6 have focused on the implementation of an improved representation of shortwave irradiances, a better characterization of factors influencing the clear sky albedo, the unification of the standard version of the model with a middle-atmosphere version, and improved model diagnostic packages. The increasing challenge of model development is reflected in the release cycle, and only 3 years separated the release of ECHAM1 from ECHAM3, a decade has passed since the release of ECHAM5.

[7] ECHAM's place in the coupled modeling system has also evolved, with interest in providing a more elaborate description of the Earth system being partly responsible for the increasing time between releases of ECHAM itself. Ocean models, which have been coupled to ECHAM, have developed considerably. Early versions of ECHAM were coupled to the large-scale geostrophic ocean model (LSG) [Maier-Reimer *et al.*, 1993] or the ocean model with isopycnal coordinates (OPYC). Later versions of ECHAM were coupled to the Hamburg ocean primitive equation (HOPE) model and its successor, the Max Planck Institute Ocean Model (MPIOM) [Marstrand *et al.*, 2003]. In addition, various threads of model development have been spawned in relation to the degree to which the middle and upper atmosphere is resolved, and the use of submodels. For instance, the middle-atmosphere version of ECHAM (MAECHAM), incorporated a much higher (0.01 hPa) model top and was used to study stratospheric variability [Manzini and Bengtsson, 1996]. The Hamburg model of the neutral and ionized atmosphere (HAMMONIA) [Schmidt *et al.*, 2006] extended ECHAM even further, to 250 km, and included radiative and dynamical processes relevant to the upper atmosphere as well as a prognostic treatment of 48 chemical compounds. At the MPI-M, an interactive aerosol model was first introduced with ECHAM4 [Timmreck, 2001], and more comprehensive approaches were developed along with ECHAM5 (e.g., Hamburg aerosol model (HAM), Stier *et al.* [2005]), and further extended to include coupled chemistry [Pozzoli *et al.*, 2008]. Starting with ECHAM5 experiments also began to incorporate a more comprehensive and dynamic treatment of land-surface

processes [e.g., *Brovkin et al.*, 2009], including the carbon cycle [*Raddatz et al.*, 2007; *Jungclaus et al.*, 2010].

[8] Over successive generations of ECHAM vertical and horizontal resolution has also increased. ECHAM1 and ECHAM2 both ran at an operational resolution of T21 (denoting a triangular truncation of the spherical harmonics to 21 wave numbers) with 19 vertical levels. ECHAM3 was the first version to run at T42, but also with 19 vertical levels. Successive versions were developed to run at higher, and more variable, resolutions. ECHAM5 was mostly run on a grid with 31 vertical levels with a horizontal resolution of T63, but much higher resolution reaching up to T319 was also used to study tropical cyclones [*Bengtsson et al.*, 2007]. By incorporating the middle-atmosphere developments associated with earlier versions of ECHAM, ECHAM6 has been developed to run on a yet more expansive vertical grid, with 47 or 95 vertical levels, and with horizontal resolutions ranging from T31 to T255.

### 3. Model Description

[9] ECHAM6 is an atmospheric general circulation model, and as such focuses on the coupling between diabatic processes and large-scale circulations, both of which are ultimately driven by radiative forcing. It consists of a dry spectral-transform dynamical core, a transport model for scalar quantities other than temperature and surface pressure, a suite of physical parameterizations for the representation of diabatic processes, as well as boundary data sets for externalized parameters, such as trace gas and aerosol distributions, tabulations of gas absorption optical properties, temporal variations in spectral solar irradiance, land-surface properties, etc. The major changes relative to ECHAM5 include: an improved representation of radiative transfer in the shortwave (or solar) part of the spectrum; a completely new description of the aerosol; an improved representation of surface albedo, including the treatment of melt ponds on sea ice; and a greatly improved representation of the middle atmosphere as part of the standard model. In addition, minor changes have been made in the representation of convective processes, and through the choice of a slightly different vertical discretization within the troposphere, as well as changed model parameters. Changes have also been made to the software infrastructure of the model to allow it to more flexibly adapt to changing computational environments, and more naturally accommodate a variety of submodels, and an expanded set of online diagnostics, including satellite simulators and point output data.

#### 3.1. Adiabatic Core

[10] The adiabatic core of ECHAM6 consists of a mixed finite-difference/spectral discretization of the primitive equations. It is identical to that employed in ECHAM5, but an overview is provided here for the reasons stated in the introduction. Because horizontal diffusion is needed for numerical closure of the dynamical core and computed in spectral space, its description is

included in this section, which otherwise is devoted to a description of adiabatic processes.

[11] Like all versions of ECHAM before it, the dynamical core of ECHAM6 is based on vorticity and divergence form of the primitive equations, with temperature and surface pressure being the thermodynamic coordinates. The spectral-transform method as implemented by the ECMWF [*Simmons et al.*, 1989, and references therein] is used to represent spatial differences over spherical surfaces (model layers). Time marching of the primitive equations is centered in time, with an Asselin filter to damp computational modes, and semi-implicit corrections to facilitate larger time steps. For the time marching of vorticity, a semi-implicit correction is implemented through a linearization of the zonal contribution to vorticity advection, with the basic state taken to be the zonally averaged zonal winds. For the time stepping of the divergence and thermodynamic equations, gravity wave contributions are represented semi-implicitly with the help of a linearization of the governing equations about an isothermal reference temperature ( $T_{\text{ref}} = 300 \text{ K}$ ) and pressure ( $p_{\text{ref}} = 800 \text{ hPa}$ ).

[12] The vertical is discretized following the method of *Simmons and Burridge* [1981] and employs a hybrid sigma-pressure coordinate system on a Lorenz grid, with pressure staggered vertically with respect to temperature (on so-called half levels), such that

$$p_{k+\frac{1}{2}} = A_{k+\frac{1}{2}} + B_{k+\frac{1}{2}} p_s, \quad (1)$$

where  $p_s$  is the surface pressure, and the coefficients  $A_{k+\frac{1}{2}}$  and  $B_{k+\frac{1}{2}}$  define the vertical grid. Pressure at full levels is specified as the arithmetic mean of the half-level pressures, and vertical advection is formulated so as to conserve potential and kinetic energy. Pressure gradients are calculated to conserve angular momentum using the perturbation virtual temperature following the formulation of *Simmons and Chen* [1991] so as to minimize errors over steep topography.

[13] Two vertical grids, L47 and L95, are emphasized in ECHAM6. They were constructed with the goal to combine the lower tropospheric resolution of the L31 grid of ECHAM5, with the vertical extent and resolution in the middle and upper atmosphere of the L39 and L90 grids used in the middle-atmosphere version ECHAM5 [*Manzini et al.*, 2006; *Giorgetta et al.*, 2006]. Both the L47 and L95 vertical grids are shown for the case of a 500 hPa mountain in Figure 1. The L47 grid is identical to the L31 grid up to 100 hPa, while the L95 grid shares the lowermost 12 levels up to 611 hPa. L47 and L95 resolve the atmosphere up to 0.01 hPa or roughly 80 km. The top-of-model pressure,  $p_{1/2}$ , is 0 hPa.

[14] Horizontal diffusion is necessary to stabilize the model; however, an attempt is made to minimize its effects by adjusting the scale selectivity (through the order of the diffusion operator) so that the strongest effects are limited to the very top of the model where the rarified atmosphere is particularly vulnerable to perturbations. This is largely an empirical exercise designed to minimize the amount of necessary diffusion to run the model stably while maintaining a time step as long



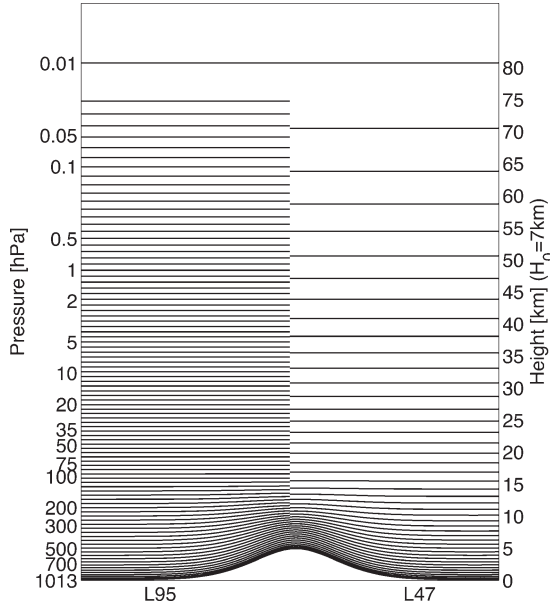


**Figure 1.** L47 and L95 hybrid vertical coordinate used in ECHAM6, shown here for the case of a 500 hPa surface pressure variation as might be associated with a large mountain.

as possible. To do so, the diffusion is formulated as a generalized form of hyperdiffusion, where the order of the diffusion operator and the diffusive time constant depend on model level and horizontal resolution. The diffusion operator is configured to reduce to a standard Laplacian form near the model top. In the troposphere, additional scale selectivity is added to the diffusion operator (by changing to a sixth-order diffusion), as shown in Table 1. The diffusive time constant, taken as the  $e$ -folding time of the largest wave number, does not depend on the model level.

[15] To represent tracer transport, ECHAM6 uses the flux-form semi-Lagrangian scheme of *Lin and Rood* [1996], which was introduced in ECHAM5. Although this scheme has nice inherent conservation properties, the different treatments of transport for surface pressure and temperature as compared to other tracers can lead to a lack of mass conservation [*Jöckel et al.*, 2001].

## 3.2. Diabatic Processes

[16] Diabatic processes are irreversible processes, often associated with small-scale fluid dynamics that cannot be explicitly represented on the model grid, and must thus be parameterized, or nonfluid dynamical aspects such as radiative transfer. ECHAM6 includes a full suite of parameterized diabatic processes, which are briefly described here. The main changes from ECHAM5 are in the treatment of solar radiative transfer and land-surface processes. Minor changes to the treatment of deep convection are also included.

### 3.2.1. Vertical Mixing

[17] Vertical mixing is conceptualized as occurring as a result of a number of distinct processes, these include: wall-bounded turbulent motions that are modeled by a

boundary layer and surface layer parameterization; free-turbulent motions; shallow, deep, and mid-level convection, which are modeled by a unified mass flux formulation; and a variety of mechanisms for the non-local transport of momentum by the gravity waves that result from flow interactions with surface features or in association with atmospheric disturbances.

#### 3.2.1.1. Turbulent Mixing

[18] The boundary layer and turbulence parameterization is based on the eddy diffusivity/viscosity approach, where the eddy viscosity consists of the product of a velocity scale and a length scale. The velocity scale is based on the square root of the turbulence kinetic energy, which is described by a prognostic equation following the description in *Brinkop and Roeckner* [1995]. This approach accounts for the effect of saturation on the relationship between fluctuations in the thermodynamic coordinates and fluctuations in density. In addition, in ECHAM6 a variance equation for the virtual potential temperature,  $\theta_v$ , has been added in a fashion that is analogous to the representation of turbulence kinetic energy, in which horizontal homogeneity is assumed so that the evolution is given as the sum of a production, vertical transport, and dissipation term, such that

$$\frac{\partial \overline{\theta_v'^2}}{\partial t} = -2 \overline{w' \theta_v'} \frac{\partial \overline{\theta_v'}}{\partial z} - \frac{\partial \overline{w' \theta_v'^2}}{\partial z} - \varepsilon_{\theta_v}. \quad (2)$$

[19] This variance is used in the triggering of deep convection. Adjustments to account for stability follow the “long-tail” formulation of *Louis* [1979], which allows for additional mixing in otherwise stably stratified situations. These changes can be motivated by a desire to incorporate effects of heterogeneity and non-stationarity, which the classical theory neglects. This choice of stability function is matched to a consistent representation of the surface exchange, in that it is based on Monin-Obukhov similarity, but uses the flux-profile relationships of *Louis* [1979], wherein fluxes are computed for each surface type within a grid cell, so that the net surface flux is the weighted average over different surface types. Gustiness, for instance associated with convective downdrafts, is not accounted for

**Table 1.** Resolution Dependence of the Formulation of Horizontal Diffusion<sup>a</sup>

Model Version	T255L95	T127L95	T63L95	T63L47
$T$	0.5	1.5	7.0	7.0
$\nabla^2$ range (Pa)	0–15	0–15	0–15	0–20
$\nabla^4$ range (Pa)	15–150	15–150	15–80	20–120
$\nabla^6$ range (Pa)	>150	>150	>80	120–300
$\nabla^8$ range (Pa)	NA	NA	NA	>300

<sup>a</sup>For the purpose of this table, the order of the operator is defined within pressure levels, in the model it is chosen based on model levels, which are converted to approximate pressures in Pascals, for the purpose of presentation. Hence, changes to the diffusion operator are confined entirely to the middle and upper atmosphere. The diffusion time constant,  $\tau$ , specifies the  $e$ -folding timescale of the largest wave number in hours.

in specifying the exchange velocity at the surface, although the surface wind is allowed to affect the roughness over the ocean through a Charnock relationship, and a prescribed minimum 10 m wind speed of  $1 \text{ m s}^{-1}$  is also applied. The choice of mixing length is critical and follows the formulation of Blackadar with an asymptotic mixing length, which matched to the nondimensional height at the surface, and a fixed value of 150 m in the boundary layer. Above the boundary layer, it decays exponentially with height so that values in the lower stratosphere approach 1 m. Hence the difference between the wall-bounded turbulent mixing and free turbulent mixing above the boundary layer is modeled entirely through the specification of the asymptotic mixing length. The depth of the boundary layer,  $h$ , is defined such that  $h = \max(h_s, h_c)$ , where

$$h_s = \frac{0.3u_*}{\min(f, 5 \times 10^{-5})}, \quad (3)$$

is a shear layer depth,  $f$  is the local Coriolis frequency, and  $u_*$  is the surface friction velocity. The convective boundary layer depth,  $h_c$ , is defined to be the height of the first level whose dry static energy exceeds the value at the lowest model level.

### 3.2.1.2. Moist Convection

[20] The parameterization of moist cumulus convection is based on the mass-flux framework developed by Tiedtke [1989], with the representation of deep convection incorporating the changes introduced by Nordeng [1994]. In addition to deep convection, shallow and midlevel convection are also parameterized, but only one convective type is allowed at any given time, with preference being given to deep convection. Given that shallow convection uses the original Tiedtke formulation, deep convection uses that of Nordeng, and mid-level convection uses again the Tiedtke formulation we refer to this as the Tiedtke-Nordeng-Tiedtke scheme, or TNT. TNT is based on a quasi-equilibrium closure for deep convection, and a moisture closure for shallow convection. The deep convective updraft mixes readily with the environment through the incorporation of an organized entrainment and detrainment term. It also includes a treatment for convective downdrafts and convective momentum transport. Other aspects of TNT are discussed in detail by Möbis and Stevens [2012], and here we only note two further points. The first is that as compared to ECHAM5, the temperature excess used to trigger convection in TNT is now related to a prognostic treatment of the temperature variance in the planetary boundary layer. Previously this temperature excess of the triggering plume was set to a fixed value, 0.5 K. Although this is a step toward a more physically consistent scheme, its overall effect on the convection is relatively minor. The second point is that four parameters within the convection scheme are used to tune the model following the procedure described by Mauritsen *et al.* [2012]. These being the rate at which condensate is converted to precipitation in the convective updrafts (CPRCON), the frac-

tion of the convective mass flux that is detrained above, rather than at, the level of neutral buoyancy (CMFCTOP), and the lateral entrainment rates of both shallow and deep convection.

### 3.2.2. Wave Action

[21] Momentum transport arising from boundary effects is parameterized using the subgrid orography scheme as described by Lott [1999], with the specification of subgrid orography following the approach developed by Baines and Palmer [1990] and the treatment of gravity waves following the approach outlined by Palmer *et al.* [1986] and Miller *et al.* [1989]. The scheme accounts for blocking by subgrid orography and removes momentum from those layers below the maximum subgrid mountain height. The triggering of gravity waves by subgrid scale orography facilitates the transport of momentum through the troposphere, with momentum deposition determined by the presence of critical levels, and the amplitude of the momentum stress scaling with the effective obstacle height that causes the initial low-level flow deflection and generates the gravity waves. The strength of the gravity wave drag from unresolved orographic sources are also tuning parameters as they impact the extratropical winds in the northern hemisphere, and thereby the ocean coupling [Mauritsen *et al.*, 2012].

[22] Vertical momentum transport resulting from unresolved disturbances in the troposphere is an important momentum source for the middle atmosphere and is parameterized following the Doppler spread theory as described by Hines [1997, 2012]. In this approach, tropospheric sources are prescribed as a function of latitude, with a source level in the lower midtroposphere (680 hPa), while the upward propagation of the gravity wave spectra and the deposition, or sink, of wave activity depends on the flow, with momentum being deposited in critical levels that depend on the wave number of the broadband gravity wave source. This parameterization has been implemented in the middle-atmosphere versions of ECHAM4 [Manzini *et al.*, 1997] and ECHAM5 [Manzini *et al.*, 2006], and by defaulting to a high top in ECHAM6, it has now become standard. As has been shown in previous work the development of realistic variability above the stratosphere benefits from this treatment of gravity waves, although the arbitrary formulation of the source remains unsatisfactory. The basic treatment of the gravity-wave source term in ECHAM6 and the other parameters in this scheme are presented in detail in H. Schmidt *et al.* (The response of the middle atmosphere to anthropogenic and natural forcing in the CMIP5 simulations with MPI-ESM, submitted to *Journal of Advances in Modeling Earth Systems*, 2012, hereinafter referred to as Schmidt *et al.*, submitted manuscript, 2012.).

### 3.2.3. Stratiform Clouds

[23] Subgrid-scale cloudiness is represented using the assumed humidity distribution function scheme developed by Sundqvist *et al.* [1989], such that cloud fraction,  $f_{\text{cld}}$ , is calculated diagnostically as a function of relative humidity,  $\eta$ , once a threshold value is exceeded ( $\eta > \eta_{\text{crit}}$ ):

$$f_{\text{cld}} = 1 - \sqrt{\frac{\eta_{\text{sat}} - \eta}{\eta_{\text{sat}} - \eta_{\text{crit}}}}, \quad \text{where} \quad \eta_{\text{crit}} = 0.7 + 0.2 \exp\left(1 - (p_{\text{srf}}/p)^4\right). \quad (4)$$

[24] The critical relative humidity, whose formulation is based on the cloud-resolving model results of *Xu and Krueger* [1991], is determined by the breadth of the assumed distribution of total water, which per the above formulation narrows as the pressure,  $p$ , decreases with altitude above its surface value  $p_{\text{srf}}$ . Generally,  $\eta_{\text{sat}}$ , the saturation humidity, is set to unity. In the presence of a temperature inversion below 700 hPa, the scheme is modified by setting  $\eta_{\text{crit}} = 0.7$  and  $\eta_{\text{sat}} = 0.9$ . This modification helps improve the representation of stratocumulus clouds, which are otherwise more poorly represented. It is motivated by an appreciation that strong humidity gradients develop in the presence of an inversion that leads to artificially low humidities below unresolved temperature inversions. A version of the cloud scheme described by *Tompkins* [2002] is also implemented. This scheme includes prognostic equations for parameters of the assumed distribution and yields a realistic present day climatology, but is not used in standard integrations because it generates a very strong climate sensitivity due to behavior that appears unrealistic, but is not well understood.

[25] Although cloud fraction is diagnosed, liquid and solid condensate are treated prognostically, and referred to as cloud water and cloud ice, respectively. The prognostic equations for cloud liquid and ice largely follow the approach described by *Lohmann and Roeckner* [1996], which accounts for the transport by the adiabatic circulations, exchange terms that convert water from one of the prognostic phases to another (and which can be associated with a variety of processes), and conversion to a large-scale precipitate phase. The large-scale (as opposed to convective) precipitate is treated diagnostically, given the conversion terms from the prognostic phases, and is obtained by integrating the conversion terms over the atmospheric column. For instance, the large-scale rainwater flux,  $P_{\text{rain}}$ , can be written as

$$P_{\text{rain}} = \frac{1}{g} \int_0^p (\mathcal{S}_{\text{aut}} + \mathcal{S}_{\text{racl}} + \mathcal{S}_{\text{mls}} - \mathcal{S}_{\text{evr}}) dp, \quad (5)$$

where the terms inside the integral are source terms, which denote the production of rain from cloud water,  $\mathcal{S}_{\text{aut}}$ , the collection of cloud water by rain,  $\mathcal{S}_{\text{racl}}$ , the melting of snow,  $\mathcal{S}_{\text{mls}}$ , and the evaporation of rain,  $\mathcal{S}_{\text{evr}}$ . A similar expression can be written down for the snow. Given the precipitation flux of rain or snow, the mixing ratio of rain or snow (the two large-scale precipitate phases) can be calculated, given the sedimentation velocity of the precipitate phase.

[26] In addition to standard microphysical processes such as diffusional growth (e.g., condensation, evaporation, sublimation) and source terms associated with

hydrometeor collisions and collections, further processes are included to represent the detrainment of hydrometeors from parameterized convection and the production of condensate as a result of turbulent mixing, the latter compensating somewhat for the simple nature of the assumed distribution function thought to underly the constant saturation variance.

[27] Some of the microphysical processes depend on the population density of cloud droplets, for instance, the production of rainwater by the self-collection of cloud water, or the freezing of ice particles. Here the population density dependence is represented by fixing the number concentration of water droplets,  $N_{\text{cld}}$  so that

$$N_{\text{cld}} = C_{\text{lt}} + (C_{\text{lt}} - C_{\text{ut}}) \exp \left[ 1 - \left( \frac{p_{\text{lt}}}{\max(10,000, p)} \right)^2 \right], \quad (6)$$

where the pressure top of the lower troposphere,  $p_{\text{lt}} = 80000$  Pa, and the drop concentration valid at pressures,  $p$  (measured in Pa), greater than this is specified to depend on whether the column is over land or ocean:

$$C_{\text{lt}} = \begin{cases} 80 \text{ cm}^{-3} & \text{over ocean and sea-ice} \\ 220 \text{ cm}^{-3} & \text{otherwise.} \end{cases}$$

[28] In the upper troposphere, the drop concentration relaxes to a fixed value,  $C_{\text{ut}} = 50 \text{ cm}^{-3}$ , irrespective of surface type. The higher droplet concentrations over land are based on the present day, and thus incorporate an anthropogenic contribution to the aerosol but are not allowed to change in time. More consistent couplings between the droplet microphysical descriptions and the cloud-active aerosol is an area of active research and development [e.g., *Stier et al.*, 2005; *Lohmann et al.*, 2007]. Although prototype schemes have been developed, the nature of the coupling between clouds and aerosol particles remains uncertain, particularly on the scale of the cloud ensemble that large-scale models endeavor to parameterize [*Stevens and Feingold*, 2009], and simple schemes that have been developed to capture these effects may not even produce the correct sign of the net interaction. For this reason, a simple approach is taken in the base version of ECHAM6, and the cloud droplet concentrations are kept fixed as described above. This implies that the adjusted forcing from aerosol cloud interactions in the ECHAM6 experiments conducted as part of the CMIP5 exercise is not allowed to change in time. For sensitivity studies, it remains possible to link a climatology of the cloud-active aerosol to the cloud droplet microphysics or even couple an interactive aerosol model.

### 3.2.4. Radiative Transfer

[29] Radiative transfer in ECHAM is represented using the rapid radiation transfer suite of models as optimized for general circulation modeling studies



(RRTM-G, *Iacono et al.* [2008]) for both the shortwave and longwave part of the electromagnetic spectrum. This is a significant departure from ECHAM5, which used the four-band model of *Fouquart and Bonnel* [1980] for the shortwave. RRTM-G takes the two-stream approach, wherein upward and downward irradiances are calculated over a predetermined number of pseudowavelengths, or  $g$ -points, an approach that is usually referred to as the correlated- $k$  method, where  $k$  denotes absorption and  $g$  indexes the cumulative distribution of absorption within a band. Quadrature is performed over 140  $g$ -points in the longwave part of the spectrum and 112  $g$ -points in the shortwave part of the spectrum. These are grouped into 16 and 14 bands, spanning the wavelength range from 10 to 3000  $\text{cm}^{-1}$  and 820 to 50,000  $\text{cm}^{-1}$  for the longwave and shortwave part of the spectrum, respectively. The optical properties for radiation are updated every 2 h, except for very high-resolution (T255) simulations for which updates are hourly. Longwave irradiance is rescaled based on surface temperature, and shortwave irradiance is rescaled by the zenith angle on time steps in between an update of the optical properties.

[30] The treatment of radiative transfer depends on a specification of the optical properties of the medium through which the radiation is passing. These come from contributions of the gaseous media, the particulate distribution, and the effects of condensate. The gaseous component trace gas concentrations are specified in ECHAM6, with the exception of water vapour, which is treated prognostically and, when run as part of the MPI-ESM,  $\text{CO}_2$ . Given the gaseous concentration, the optical properties at the different  $g$ -points are interpolated from tabulated values and vary with ambient pressure, and in some cases are modified by the presence of other trace gases. The optical properties of the aerosol are prescribed from a new climatology developed by S. Kinne et al. (A new global aerosol climatology for climate studies, submitted to *Journal of Advances in Modeling Earth Systems*, 2012, hereinafter referred to as Kinne et al., submitted manuscript, 2012), which is summarized in section 3.4. Cloud optical properties are calculated for each band using Mie theory, and the prognosticated condensate amount coupled to an assumed size distribution from which the effective radius,  $r_e$  in microns, of cloud liquid and ice is calculated as follows

$$r_{e,l} = \kappa \left( \rho \frac{q_l}{N_{\text{cld}}} \right)^{1/3} \quad \text{and} \quad r_{e,i} = 83.8 q_i^{0.216}, \quad (7)$$

where  $q_l$  and  $q_i$  denote the mixing ratios of the condensate phases, and  $\rho$  is the liquid water density, and  $\kappa$  parameterizes the breadth of the droplet distribution. The formulation for water droplets varies over land and the ocean through the variation in  $N_{\text{cld}}$ , which is as described from the microphysics and also through changes in  $\kappa$  which is set to 1.143 over land where the droplet distribution is generally narrower and 1.077 over ocean. The calculation of the effective diameter is

unchanged from ECHAM5 but the conversion between effective diameter (or radius) and condensate amount, to cloud optical properties is now based on revised Mie calculations that take into account the band structure of RRTM-G.

[31] To capture the optical properties of clouds in ECHAM6, different approaches are used in the longwave and shortwave portions of the spectrum. In the shortwave, a lookup table provides spectral varying single scattering properties at all central wavelengths of the 14 spectral subbands. The lookup table is based on Mie simulations [Dave, 1968]; thus, a spherical particle is assumed. The needed refractive indices in these simulations are based on data by *Hale and Querry* [1973] for liquid water and *Warren and Brandt* [2008] for ice. The cloud particle size distribution is assumed to be log-normal and for purposes of computation is discretized into 61 equally sized bins, from 2 to 32  $\mu\text{m}$  and from 4 to 124  $\mu\text{m}$  for liquid and ice particles, respectively. The standard deviation, describing the size-distribution width, increases with size from 1.200 (at the smallest size) to 1.444 (at the largest size) for both condensate classes. For ice particles, the nonsphericity impacts on solar scattering (e.g., increased side scatter) imply that both the cosingle scattering albedo and the asymmetry factor need to be reduced. The reduction in absorption is tied to ice mass estimates, which involves the lower (than water) ice density  $0.917 \text{ g cm}^{-3}$  and a factor

$$\left( 1 + 0.01 \frac{r_{e,i}}{2 \mu\text{m}} \right)^{-1},$$

[32] which approximates expected reductions in ice density (e.g., complex structures, hollow elements) with increasing ice-crystal size (measured in microns). The solar asymmetry factors for ice,  $g_i$ , are reduced relative to their value of spherical water droplets,  $g_l$ , by a simple parameterization  $g_i = 1.3g_l / (2.3 - g_l)$ .

[33] In the longwave, the cloud optical properties are the same as was implemented in ECHAM5 [Roeckner et al., 2003]. For a given grid-cell condensate path,  $\chi$ , the homogeneous optical depth,  $\tau_h$ , is given as  $\tau_h = 1.66k\chi$ , where 1.66 is a diffusivity factor, and  $k$  is a mass absorption coefficient parameter. For liquid water clouds

$$k = c + d_1 \exp(-d_2 r_{e,l}), \quad (8)$$

with  $c$ ,  $d_1$ , and  $d_2$  constant parameters. For ice clouds, the mass absorption parameter follows the specification of *Ebert and Curry* [1992] wherein

$$k = a_\lambda + b_\lambda r_{e,i}^{-1}, \quad (9)$$

with  $a_\lambda$  and  $b_\lambda$  being specified independently for each of the 16 RRTM spectral bands.

[34] ECHAM6 continues to use the same, maximum-random, cloud overlap as was used in ECHAM5, and three-dimensional effects continue to be parameterized

through a cloud inhomogeneity parameter,  $\zeta \in [0, 1]$ , which rescales the homogeneous cloud optical depth,  $\tau'_h$ , such that  $\tau = \zeta \tau_h$ . Mixing rules for combining the optical properties for ice and liquid within a grid cell are based on  $\tau_h$ . The radiative effects of the precipitate phases (rain and snow) are neglected.

[35] The treatment of surface albedo has also been substantially changed in ECHAM6. A new land-albedo scheme has been developed and is evaluated by V. Brovkin et al. (Evaluation of vegetation cover and land-surface albedo in MPI-ESM CMIP5 simulations, submitted to *Journal of Advances in Modeling Earth Systems*, 2012, hereinafter referred to as Brovkin et al., submitted manuscript, 2012). A melt-pond scheme for the sea-ice model has also been incorporated as described by Roeckner et al. [2012], although, in the simulations presented here, the coupling of the melt ponds to the sea ice was not properly implemented. This implementation error, or bug, acted to damp the effect of the melt ponds, which would in principle artificially reduce the surface albedo feedback; although subsequent tests have shown the effect on the CMIP5 simulations to be very small [Roeckner et al., 2012].

[36] Over the ocean, ECHAM5 treated the surface albedo as a constant, with a value equal to the globally averaged value of 0.07. In ECHAM6, the ocean albedo has been modified to account for a zenith angle dependence and to differentially treat the contribution from the near infrared versus the visible part of the shortwave spectrum for the case of direct radiation. The treatment of diffuse radiation remains unchanged. The albedo of seawater is, for the direct beam, specified as

$$A_{\text{vis}} = \frac{0.026}{\mu^{1.7} + 0.065} + 0.15(\mu - 1)(\mu - 0.5)(\mu - 0.1) + 0.0082, \quad (10)$$

where  $\mu$  is the cosine of the zenith angle. The near-infrared albedo,  $A_{\text{nir}}$ , is taken to equal  $A_{\text{vis}} - 0.0152$ . Following (10) at a zenith angle of zero,  $\mu = 1$  and  $A_{\text{vis}} = 0.0326$ .

### 3.3. Land-Surface Model (JSBACH)

[37] JSBACH is based on a tiling of the land surface and includes dynamic vegetation with 12 plant functional types and two types of bare surface. Land-surface albedo is calculated separately for the visible and near infrared, and includes a consideration of the bare surface fraction, snow on soil, and canopy effects, including forest masking. The soil hydrology is described by a simple single-layer bucket model, and temperatures are modeled over five soil layers. A detailed technical description of the landcover parameterization is given in (C. Reick et al., Landcover changes in MPI-ESM CMIP5 simulations, submitted to *Journal of Advances in Modeling Earth Systems*, 2012) and evaluated in Brovkin et al. (submitted manuscript, 2012).

### 3.4. Prescribed Data

[38] Integration of ECHAM6 is dependent on a variety of prescribed data. This includes trace gas concentrations, the aerosol, the surface orography and its

subgrid scale representation, land-surface (for instance, soil type) and vegetation climatologies (in the case they are not predicted), and in the case of simulations using fixed sea-surface temperatures (SSTs), a specification of SSTs and sea-ice coverage.

[39] The gas climatologies of  $\text{CO}_2$ ,  $\text{CH}_4$ ,  $\text{N}_2\text{O}$ , and chloroflourocarbons (CFCs) are specified by a single value meant to be representative for the tropospheric concentration. The  $\text{CO}_2$  concentration, if not computed prognostically in the fully coupled MPI-ESM model, is assumed to be constant in the whole model atmosphere.  $\text{CH}_4$  and  $\text{N}_2\text{O}$  are homogeneously mixed in the troposphere and lower stratosphere, and then decay to background values typical for the mesosphere. Water vapor concentrations in the middle atmosphere are also influenced by parameterized photodissociation and oxidation of methane, as described in more detail in Schmidt et al. (submitted manuscript, 2012). The default ozone climatology is given as three-dimensional monthly values, although in the stratosphere, ozone is assumed to not vary with longitude, and is based on the merged and future ozone climatology as described by Cionni et al. [2011] for CMIP5. The original data, however, cover only altitudes up to 1 hPa and have been extended upward for use in ECHAM6 as described by Schmidt et al. (submitted manuscript, 2012).

[40] The stratospheric aerosol is based on an extension of the Pinatubo aerosol data set [Stenchikov et al., 1998] to cover the entire period between 1850 and 1999. Its application in ECHAM6 is also described further by Schmidt et al. (submitted manuscript, 2012). The tropospheric aerosol is described by a fine and a coarse mode, with a separation radius of  $0.5 \mu\text{m}$ . Coarse-mode aerosols are assumed to be of natural origin, comprising dust and sea salt. Fine-mode aerosol consists of a mixture of natural and anthropogenic aerosols and consists of sulfate and organic matter, including black carbon. The basic climatology is given by two-dimensional maps of aerosol optical depth, single scattering albedo and Ångström exponent, which are then distributed in the vertical using the profiles derived from the ECHAM5-HAM model. The split between fine- mode and coarse-mode aerosol is facilitated by the Aeronet data, which is also used to calibrate the climatology as a whole. The fine-mode contribution can be related to estimates of past emissions so as to allow an historical reconstruction of anthropogenic contributions to the aerosol, as well as projections associated with future scenarios, and thereby allows for a consideration of the contribution of the aerosol to radiative forcing. Further details about the aerosol climatology are provided by (S. Kinne et al., A new global aerosol climatology for climate studies, submitted to *Journal of Advances in Modeling the Earth System*, 2013).

[41] Detailed information about the subgrid orography is required by the parameterization for subgrid orographic drag and wave generation. In all, seven parameters are required: the standard deviation, the anisotropy, the maximum elevation, the minimum elevation, the mean slope, the mean orientation, and the mean elevation of the orographic features within a grid



cell. These are derived from the 10-min topographic data set provided by the U.S. navy, and the relationships provided by *Baines and Palmer* [1990]. For simulations with fixed sea-surface temperatures, the data are taken from the Program for Climate Model Diagnosis and Intercomparison (PCMDI) archive for the historical period, and bilinearly interpolated to the ECHAM6 grid.

[42] The CMIP5 Atmospheric Model Intercomparison Project (AMIP) simulation was run with land-use transitions and prescribed distribution for natural vegetation. Only three types of land-surface climatological data entered these simulations: soil albedo, crop fractions, and the field capacity of the soil. The soil albedo is read from static maps derived from the Moderate Resolution Imaging Spectroradiometer (MODIS) data set MOD43C1 (for white sky albedo) and MOD15A2 (for the fraction of absorbed photosynthetically active radiation) for the period 2001–2004. To derive the full-surface albedo requires the vegetation albedo which is also derived from those MODIS data, but transformed into a single value for each plant functional type. The cover fractions of crops and pastures follow the New Hampshire harmonized protocol for CMIP5 [*Hurt et al.*, 2011], the remaining part of the grid cells is covered by natural vegetation based on *Ramankutty and Foley* [1999], the reclassification to the JSBACH plant functional type is explained in *Pongratz et al.* [2008]. The map of the field capacity of the soil is described in *Hagemann* [2002]. For most of the other CMIP5 simulations, the situation is the same, except that the natural vegetation mentioned in relation to the derivation of crop cover fractions is computed interactively.

### 3.5. Errata

[43] In the course of evaluating the MPI-ESM and ECHAM6 simulations as part of CMIP5, a number of bugs have been identified which impact simulations. In addition to the melt-pond bug discussed above, several further bugs have been identified and merit mention.

[44] In implementing the new-aerosol climatology, a data-formatting error led to a somewhat weaker anthropogenic aerosol forcing than was foreseen in the original data set, with the effect most pronounced over the heavily populated regions of the northern hemispheric continents. The adjusted all-sky aerosol forcing for the AMIP period, calculated as the difference between the top-of-atmosphere (TOA) fluxes for the AMIP period with the aerosol load for this period (including the formatting bug) and a run for the same period but with the preindustrial tropospheric aerosol loading is  $-0.34 \text{ W m}^{-2}$ . If the calculation is repeated but with the formatting bug removed, the adjusted forcing increases to  $-0.50 \text{ W m}^{-2}$ . For reference, the difference in the clear sky shortwave-adjusted forcing between the two simulations is nearly three times as large ( $0.42 \text{ W m}^{-2}$ ), suggesting that much of the missing forcing attributable to the formatting error is offset by additional adjustments, compensating effects in the longwave, and cloud-masking effects. Use of the correct aerosol only has a small impact in the representation of the clear sky-reflected solar irradiance, decreasing the root-mean-square error (RMSE) relative to Clouds and

Earth's Radiant Energy System (CERES) from 6.6 to  $6.5 \text{ W m}^{-2}$ .

[45] In contrast, small inconsistencies in the representation of cloud processes have a much larger effect. Earlier versions of ECHAM6 do not conserve energy, neither in the whole nor within the physics, and small departures from water conservation are also evident. Analysis of the CMIP5 runs suggest that these issues persist with ECHAM6. Since the CMIP5 runs, an attempt has been made to identify the origin of departures from mass and thermal energy conservation within the framework of the ECHAM6 single column model. A variety of model errors relating to the inconsistent use of specific heats, how condensate was passed between the convection and cloud schemes, or how vertical diffusion was represented over inhomogeneous surfaces have been identified and corrected. In addition, analysis of high-frequency CFMIP output helped identify an error in the cloud scheme, which favored cloud fractions of zero or unity. These errors predate the developments of ECHAM6, and they individually change the top of the atmosphere energy balance by anywhere from a few to as much as  $15 \text{ W m}^{-2}$  for the case of the cloud-scheme error, thus illustrating how model tuning as a rule compensates biases in parameterizations of clouds and in their implementation. These biases in clouds can be 2 orders of magnitude larger than the biases associated with a poor representation of aerosol effects.

[46] In the process of optimizing the model, a bug was introduced in the gravity wave parameterization, which influences the momentum deposition in the upper atmosphere. This leads to small asymmetries emerging in otherwise symmetric aquaplanet configurations of the model, where differences that are significant at the 95% level are evident in the strength of the jets (a  $2 \text{ m s}^{-1}$  difference is evident in the strength of the zonal winds in the upper troposphere at  $60^\circ\text{S}$ ) and in the strength of the polar vortex. Differences in the sea-level pressure at  $60^\circ\text{S}$  are on the order of 1–2 hPa between the AMIP simulations and AMIP simulations in which the bug was corrected. The bug also affects the period of the quasibiennial oscillation (QBO), so that the gravity wave sources would have to be retuned to maintain a good representation of the QBO in the mixed resolution (MR) configuration of ECHAM6 without the bug.

### 3.6. Model Configurations and Experiments

[47] Although the entire model development process is one that takes into account how changes in the model impact its ability to represent the observed climate system, some parameters are further adjusted after the model physics is frozen so as to optimize its performance (as measured against the present climate) for a given resolution. Five of these parameters control the strength of the gravity wave drag originating from unresolved orographic sources. Two further parameters originate through the convective parameterization: one which controls the detrainment of cloud water above the level of neutral buoyancy; another which controls the rate at which cloud water in the convective updrafts

**Table 2.** Parameter Values for Different ECHAM6 Configurations<sup>a</sup>

Version	Truncation	Levels	Time Step	CMFCTOP	CPRCON	GKDRAG	GPICMEA	RMSCON_LO
CR	T031	47	20 min	0.210	2.0	NA	NA	NA
LR	T063	47	10 min	0.210	2.0	0.50	400	1.20
MR	T063	95	10 min	0.2	2.0	0.25	400	1.20
HR	T127	95	5 min	0.205	1.3	0.25	100	1.05
XR	T255	95	2 min	0.205	1.3	0.25	100	1.05

<sup>a</sup>The truncation measures the horizontal resolution, which is measured by the number of wave numbers in the triangular truncation of the spherical harmonics. Vertical resolution is determined by the number of model levels. Key resolution-dependent parameter settings for various ECHAM configurations include: CMFCTOP is the fraction of air detrained above the level of neutral buoyancy, CPRCON denotes the conversion rate of cloud water to precipitation in convective updrafts, and the remaining parameters control the strength of the momentum transport by gravity waves caused by unresolved topography.

is converted to precipitation. All, but particularly those related to the effect of subgrid orography on gravity waves, are plausibly related to model resolution, but their identification as tuning parameters also reflects their effectiveness in controlling important aspects of the climate. Parameter settings are given in Table 2, where only three of the gravity wave parameters are shown; the remaining four are formulated as a function of those listed. The physical interpretation of these parameters is presented in the model description section above, and a more extensive discussion of the role of these parameters and how the model was tuned is provided in a companion paper [Mauritsen *et al.*, 2012].

[48] Five different resolutions of ECHAM6 have been tuned (Table 2), ranging from a coarse resolution (CR) model, which is primarily used for teaching purposes, to a very high resolution (HR) model which is used for exploratory studies. Only the CR, LR, and MR models () have been successfully coupled to the ocean model in a way that produces a stable climate. For fixed sea-surface temperatures, the HR model has, in many respects, the best climate. But when coupled to the ocean, it produces an Atlantic meridional overturning circulation that is too weak, which (for reasons not understood) leads to large biases in the north Atlantic region, and as a result, a less satisfactory overall climate. For this reason, the coupled work has focused on the LR and MR configurations. Exploratory work with a experimental very high resolution (XR) configuration of ECHAM6 is also included, although its climate has been less extensively investigated. Simulations with various versions of ECHAM6 are compared to simulations by earlier versions of ECHAM dating back to ECHAM3. Because old versions of ECHAM are not systematically ported to new machines the comparison is based on existing

AMIP simulations, which because they were conducted in the past simulate a shorter period of time as indicated in Table 3. Throughout the remainder of this document, the naming convention?R (where ? is either C, L, M, H, or X) is used to refer to various configurations of ECHAM6, and E# (where # is either 3, 4, or 5) is often used in the annotation of figures as shorthand for denoting simulations by an earlier ECHAM version, i.e., following Table 3.

[49] Because this paper focuses on the behavior of the atmospheric model, we focus our attention on experiments that use a prescribed SSTs, namely the AMIP experiments that are defined in the CMIP5 protocol. Doing so also provides more opportunity to compare the model to earlier versions of ECHAM. Table 4 summarizes the simulations that are analyzed in this overview paper. For the AMIP simulations, the periods are progressively longer for later versions of ECHAM, as archived simulations from earlier model versions are used as a basis of comparison. Other forcings, such as the aerosol, solar forcing, and ozone climatology, also change across AMIP simulations stemming from different model versions, although it is assumed in this analysis that such changes are not decisive. In addition to AMIP, and AMIP-like simulations, several coupled simulations are also analyzed, including the preindustrial control, the historical, and the abrupt4×CO<sub>2</sub> simulations, as this was necessary to estimate basic properties, such as the climate sensitivity, of the atmospheric model. Emphasis is placed on documenting basic elements of the behavior of ECHAM6, rather than exhaustively documenting the properties of any particular configuration. Although results from the LR configuration (which

**Table 3.** Naming Conventions and Model Configurations Analyzed in This Study

Name	Model Version	Configuration	AMIP Period	Realizations
E3	ECHAM3	T042L19	1979–1989	1
E4	ECHAM4	T042L19	1979–1993	1
E5	ECHAM5	T063L31	1979–1999	1
LR	ECHAM6	T063L47	1979–2008	3
MR	ECHAM6	T063L95	1979–2008	3
HR	ECHAM6	T127L95	1979–2008	1
XR	ECHAM6	T255L95	1979–2008	1

**Table 4.** Additional CMIP5 Experiments Analyzed in This Study<sup>a</sup>

Experiment	Brief Description
piControl	1000 year control run with preindustrial forcings
abrupt4×CO <sub>2</sub>	150 year simulation with fourfold increase in CO <sub>2</sub>
Historical	1850–2000 with best estimate of historical forcings
AMIP	AMIP (prescribed SSTs and Sea ice, 1979–2008)
AMIP4×CO <sub>2</sub>	AMIP with fourfold increase in CO <sub>2</sub>
climSST	AMIP like with climatological SSTs from piControl
climSST4×CO <sub>2</sub>	climSST with fourfold increase in CO <sub>2</sub>

<sup>a</sup>All experiments were simulated by ECHAM6 MR and LR for the AMIP and AMIP-like runs or the MPI-ESM-LR and MPI-ESM-MR for the coupled runs.

**Table 5.** Energy Budget Terms Estimated From Observations and From ECHAM

		Historical			AMIP			AMIP		
SS12		LR	MR	LR	MR	HR	XR	E5	E4	E3
<i>Top of Atmosphere</i>										
SW Dn	340	340.4	340.4	340.4	340.4	340.4	340.4	341.3	341.2	341.0
SW Up	100	102.9	100.9	103.0	101.0	100.2	98.7	106.7	104.3	104.2
LW Up	239	236.4	238.4	236.9	238.5	239.6	241.5	232.8	235.3	233.3
<i>Surface</i>										
$T_s$	NA	287.4	287.6	287.7	287.7	288.3	288.4	288.3	287.9	287.8
SW Dn	187	186.0	188.1	185.9	188.3	190.2	192.4	183.1	171.1	190.7
SW Up	25	24.2	24.4	24.8	25.1	25.5	25.8	25.0	23.3	24.5
LW Dn	342	341.1	341.6	344.3	343.2	341.6	339.7	343.6	344.3	333.7
LW Up	397	397.0	398.1	399.1	398.9	398.7	398.8	398.3	396.9	396.9
LHF	86	84.9	86.3	86.0	86.8	86.9	87.4	84.5	81.6	80.2
SHF	20	19.7	19.7	19.6	19.7	19.6	19.1	17.4	11.9	13.2
<i>Net Absorbed</i>										
TOA	1	1.1	1.2	0.5	0.9	0.6	0.2	1.9	1.6	3.5
Surface	1	1.4	1.3	0.8	1.1	1.1	1.0	1.7	1.7	1.2
LHF+SHF	106	104.6	106.0	105.6	106.5	106.5	106.5	101.8	93.5	93.2

SS12 estimates are from *Stevens and Schwartz* [2012], who do not separate the upward and downward contributions to the net surface shortwave irradiance, which they estimate at  $162 \text{ W m}^{-2}$ , with a range of  $23\text{--}30 \text{ W m}^{-2}$  for the upward surface SW irradiance. They also indicate an uncertainty of more than  $\pm 5 \text{ W m}^{-2}$  for the surface energy budget terms, and less than  $\pm 2 \text{ W m}^{-2}$  at the top of the atmosphere. SW, shortwave irradiance; LW, longwave irradiance; LHF, the heat flux from evaporation and sublimation; SHF, the sensible heat transfer from the surface.

because it is cheaper to run is more likely to be used more extensively) are used to illustrate the behavior of ECHAM6, if this behavior is resolution dependent, then other model configurations will be documented as well.

## 4. Climate

[50] In this section, the climate of ECHAM6 is described, and compared when appropriate to the climate of previous versions of ECHAM. Given that the main changes in the development of ECHAM6 have had to do with the representation of surface albedo, the aerosol, and shortwave radiative transfer, somewhat more focus is placed on a discussion of the energy budget and clouds as compared to other aspects of the climate system.

### 4.1. Energy Budget

[51] The energy budget for different ECHAM configurations is provided for reference in Table 5. For the model configurations used in the MPI-ESM, both the energy budget from simulations with the coupled model over the latter part of the historical record (1979–2005) and from AMIP simulations are provided. AMIP simulations, by virtue of their fixed sea-surface temperatures and sea-ice concentrations, do not have a closed energy budget, but they prove to be a good indicator of the behavior of the coupled model over the latter part of the historical period. Hence, they are included as a basis for comparing the atmosphere models across resolutions, where we do not have coupled simulations, and to earlier model versions.

[52] Among the different terms in the energy budget, the net rate of cooling in the atmosphere has seen a pronounced change over various versions of ECHAM, with progressively less absorption of shortwave irradiance by the atmosphere, both as a result of improved spectral resolution in the radiative transfer and an

improved aerosol climatology. Enhanced cooling in the atmosphere is accompanied by more precipitation, or equivalently surface evaporation, as condensational heating is the principle term balancing radiative cooling in the atmosphere. In addition to an increase in precipitation by about 5%, newer generations of ECHAM also exhibit a systematic shift to higher surface Bowen ratios. ECHAM3 and ECHAM4 had a Bowen ratio of about 0.15, as compared to 0.23 for ECHAM6.

[53] Differences in the energy budget at the TOA and the surface are also evident across the generations of ECHAM. Such differences, if real, would imply either that the atmosphere is heating or cooling over the analysis period or that the atmosphere does not conserve energy identically. The latter is known to be an issue in ECHAM, but the diagnosis is also limited by a failure to consider snow melt. If all the snowfall that reached the surface in ECHAM were to melt, this would reduce the net surface heat flux by about  $0.7\text{--}0.75 \text{ W m}^{-2}$  of energy. Because not all snow melts, some accumulates and some sublimates, only part of this can contribute to the surface energy budget. For later model versions in which there is an imbalance between the TOA and the surface of between  $0.8 \text{ W m}^{-2}$  (XR) and  $0.1 \text{ W m}^{-2}$  (MR-historical), it seems likely that a few tenths of a Watt per square meter in the discrepancy can be explained by a failure to consider melting snow, the remainder is likely due to energy imbalances in the atmosphere.

[54] Changes to the aerosol climatology, and to the surface albedo, also lead to significant improvements in the simulation of clear sky radiation by the ECHAM6 relative to ECHAM5. The RMSE of the annually averaged data decreases from  $7.3 \text{ W m}^{-2}$  for ECHAM5 to  $6.6 \text{ W m}^{-2}$  in ECHAM6-LR. Overall, the tropical regions reflect less shortwave irradiance, and biases over north Africa and the equatorial Atlantic have been significantly reduced (Figure 2). Large biases remain



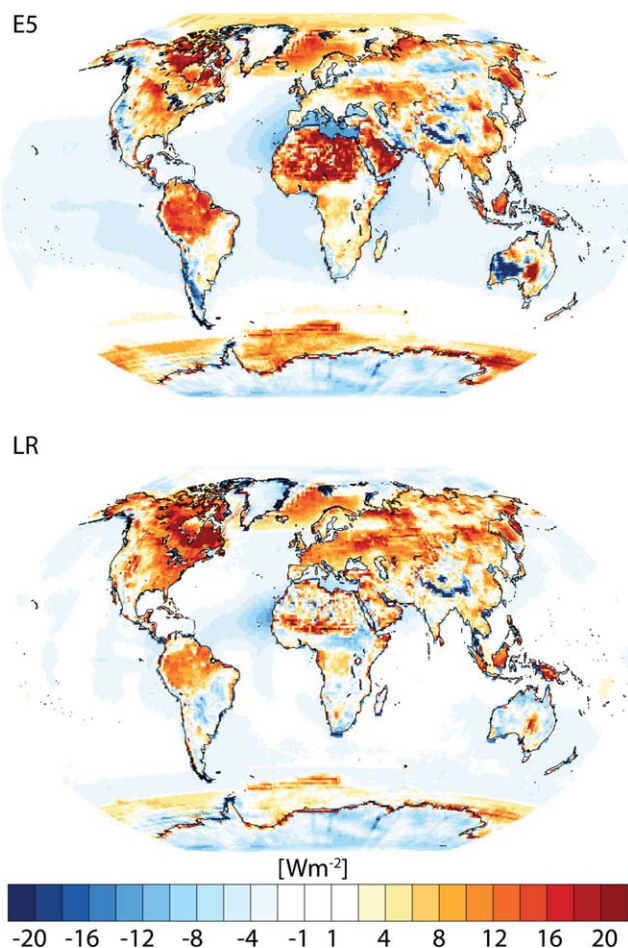


**Figure 2.** Difference between observed (CERES Edition 2.6r) and simulated reflected shortwave irradiance at top of atmosphere, for (upper) ECHAM5 and (lower) ECHAM6-LR. RMSE differences are  $7.3 \text{ W m}^{-2}$  for ECHAM5 and  $6.6 \text{ W m}^{-2}$  for ECHAM6-LR. Mean biases which are similar,  $2.6 \text{ W m}^{-2}$  for both models, are removed before plotting, and the sign convention is chosen such that a positive difference indicates too little reflected (hence more absorbed) shortwave radiation, and is colored with warmer (redder) colors.

over the continents. These are for the most part consistent with the biases identified by Brovkin et al. (submitted manuscript, 2012), who examined shortwave irradiance contributions to the surface energy budget error as compared to estimates of the surface irradiance taken from MODIS, except over the Amazon region of South America, where the present analysis suggests that the net downward shortwave irradiance is too large at the TOA, although the MODIS analysis suggests that it is too small. Differences between the simulations and the observed outgoing solar irradiance are much larger than what can be explained by the radiative effects of aerosols. Over the tropical ocean, the LR results show a hint of a large-scale wave number 12 standing wave. This feature is believed to be caused by the zenith angle dependence of the albedo in the radiative transfer calcu-

lation, which is only called every 2 h. Although shortwave irradiances are rescaled at each time step based on the local zenith angle, the effect of the zenith angle on albedo is not corrected for. Notwithstanding these caveats, the changes to the representation of shortwave radiative transfer, and the parameters that influence it, lead to a more skillful simulation of the spatial and temporal patterns of reflected shortwave irradiance in ECHAM6, which determines the effective solar driving of the climate system.

[55] Improvements in the spatial distribution of the annual climatology of shortwave and longwave radiation at TOA are illustrated with the help of Taylor diagram (Figure 3). To construct this diagram, the area-weighted root-mean-square difference between the annual climatology of ECHAM and CERES is decomposed by the amplitude and correlation between ECHAM and CERES (the reference) [Taylor, 2001]. Improvements are measured by a decrease in the distance to the reference point, here denoted CERES, and are most marked at higher resolution, particularly in the shortwave. There is less evidence of systematic improvements, or changes, in the representation of outgoing longwave irradiance across ECHAM versions, although this quantity is more strongly controlled by meridional temperature gradients and is, to begin with, far better simulated than is the shortwave irradiance.

[56] Overall, the different terms in the model energy budget lie within the uncertainty range of the observations, as for instance summarized by Stevens and Schwartz [2012], but this should come as no surprise as model parameters were adjusted to achieve this level of agreement at the top of the atmosphere, and at the surface, the measurements are not sufficiently discriminating.

## 4.2. Clouds and Radiation

[57] There is some indication that improvements in the representation of reflected shortwave irradiance can be attributed to clouds. Figure 4 shows the biases in the reflected shortwave irradiance for different ECHAM versions. Improvements in ECHAM6 relative to ECHAM5 become evident at higher resolution and are dominated by an improved simulation of the northern hemisphere, including the northern Intertropical Convergence Zone (ITCZ) region. Here we note that the most marked improvement was in transitioning between ECHAM4 and ECHAM5, and that biases in the southern hemisphere, with too much downward irradiance into the southern polar oceans, and too much reflected irradiance around  $40^\circ\text{S}$  are largely unchanged relative to ECHAM5. These biases in the southern hemisphere extratropics are characteristic of most models [Trenberth and Fasullo, 2010]. In ECHAM, they likely result from biases in the southern hemisphere storm tracks, which are too equatorward, combined with an overall poor representation of stratiform clouds in shallow marine boundary layers.

[58] The marine boundary layer cloud bias is a longstanding issue in ECHAM. Its signature is evident in Figure 4, wherein too much shortwave radiation is absorbed in the tropical regions, except at the ITCZ. In

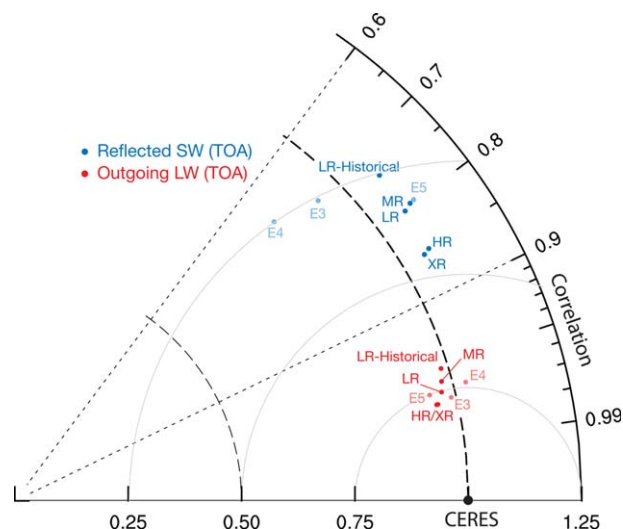


**Figure 3.** Taylor diagram of the annually averaged outgoing shortwave and longwave irradiance at the top of the atmosphere for various configurations of ECHAM with CERES Ed2.6r data as the reference data.

earlier versions of ECHAM, this bias was partially masked by an underlying surface that was too bright in the tropical regions and more reflecting aerosol particles, e.g., Figure 2. Changes in the ocean albedo in the tropical belt range from 2% to 3% in absolute terms over the annual average, and hence could explain the increased biases in absorbed shortwave radiation in the tropical regions, Figure 4. Figure 2 also suggests that there is some improvement in the representation of tropical cloudiness at higher resolution, as the zonally averaged shortwave absorption biases are substantially reduced in the HR, as compared to the LR configuration of ECHAM6.

[59] Biases in tropical cloudiness, most evident in the simulations with the LR configuration of ECHAM6, are prominent in the major stratocumulus regions, which continue to be poorly simulated with far too little cloud, as compared to what is observed. Figure 5 presents the LR lidar-cloud amount derived from the lidar simulator implemented in ECHAM as part of COSP (the CFMIP (Cloud Feedback Model Intercomparison Project) Observational Simulation Package) [Bodas-Salcedo *et al.*, 2011], alongside of the observed cloud amount reported by GOCCP. GOCCP is the GCM-Oriented CALIPSO Cloud Product [Chepfer *et al.*, 2010]. Differences between the LR and GOCCP data are as large as 0.5. Within Earth's most prominent stratocumulus region, the eastern boundary current region of the southeast Pacific, the GOCCP reports a cloud fraction approaching 0.8 as compared to 0.3 as simulated by the LR configuration of ECHAM6. By comparison biases over the Southern Ocean are much less, but show up more prominently in the zonal averages because they are zonally more extensive. As previously discussed (section 3.5), some of these deficiencies appear to be related to a longstanding bug that has caused successive generations of ECHAM to underre-

present fractional cloudiness. Tests with newer versions of the model in which this bug has been eliminated show substantial improvements in the amount of low-level tropical clouds.

[60] ECHAM6 simulates too few clouds at low level and midlevel, but those that it does simulate are too bright. This is evident in the cloud height and optical depth histograms that are produced with the incorporation of the International Satellite Cloud Climatology Project (ISCCP) [Rossow and Schiffer, 1999] simulator in ECHAM, and which facilitates comparison to the ISCCP observational products. Overall, the frequency of cloud occurrence at all levels below 300 hPa is smaller in ECHAM6 than what is observed by ISCCP, but the mode of the distribution is consistently shifted

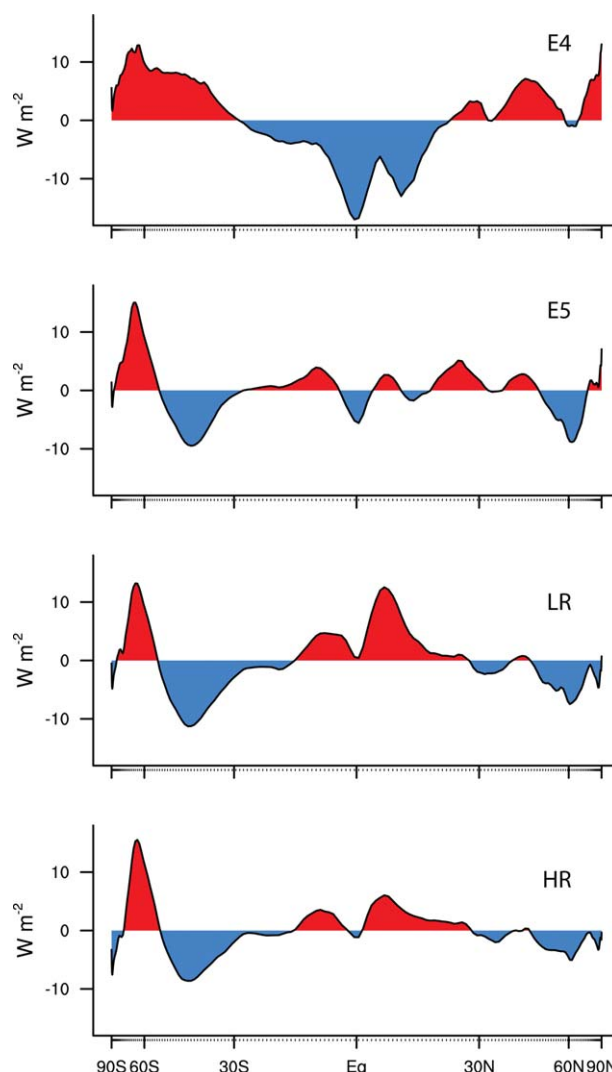


**Figure 4.** Differences between observed (CERES Ed2.6r) and simulated upward shortwave irradiance at TOA for three model generations (with two resolutions for ECHAM6). Fields are zonally and annually averaged and the mean bias is set to zero. Positive (red) regions indicate too much absorbed shortwave irradiance by the simulations.



toward higher cloud optical depths, Figure 6. These biases compensate one another to some extent, but even so a poor representation of low clouds can lead to regional biases in the radiative forcing of many tens of watts per square meter. There is also the suggestion, e.g., Figure 6, that ECHAM6 simulates too many high clouds, and those that it does simulate are too thin, but this inference may also be an artifact of ISCCP not being sensitive to high clouds with an optical depth smaller than 0.3.

[61] In summary, there is evidence of incremental improvement in the ability of ECHAM to represent major features of the observed climatology of clouds, large biases remain. In this respect, ECHAM is similar to many other state-of-the-art general circulation models (cf., *Zhang et al.* [2005] and S. A. Klein et al., Are climate model simulations of clouds improving? An evaluation using the ISCCP simulator, submitted to *Journal of Climate*, 2012).

#### 4.3. Precipitation

[62] The total amount of precipitation in ECHAM6 is about 10% larger than what is reported by the Global

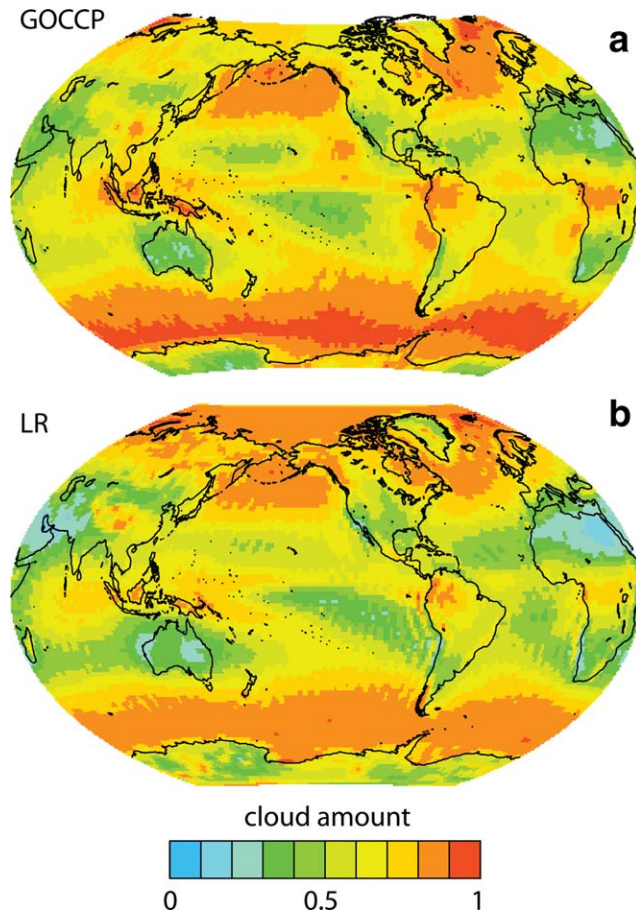


**Figure 5.** Cloud climatology as seen from space from a downward looking lidar. (a) GOCCP analysis of measurements made by CALIPSO [Winker et al., 2010]; (b) LR-AMIP climatology based on the CALIPSO simulator for the period 1980–2005.

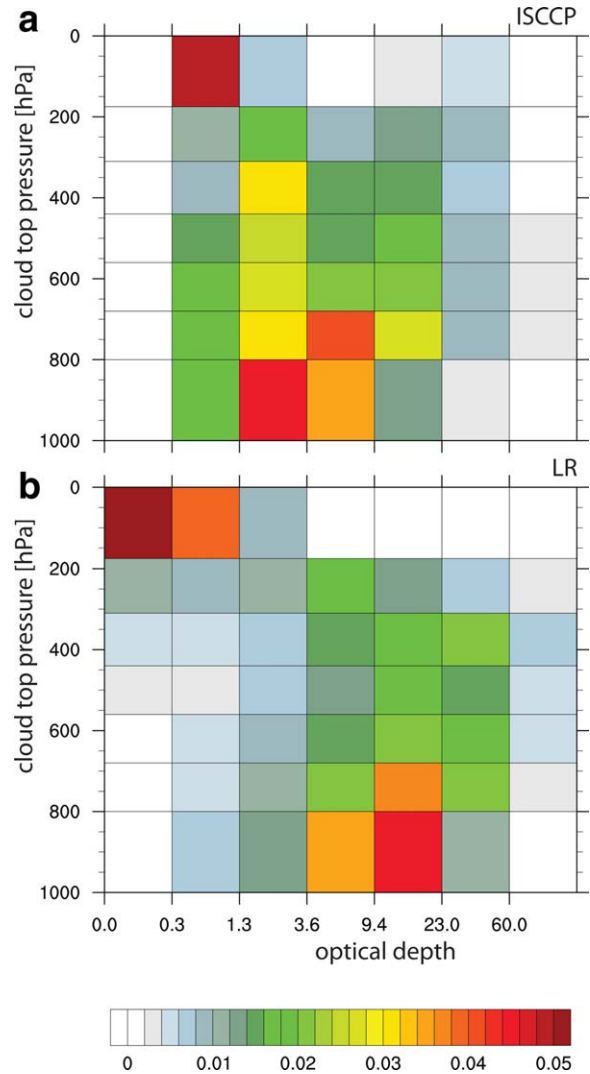


**Figure 6.** Cloud histogram showing the frequency of occurrence of cloudiness in optical thickness/cloud-top-pressure space for the period 1980–2005: (a) ISCCP; (b) LR-AMIP climatology based on the ISCCP simulator.

Precipitation Climatology Project (GPCP) [Adler et al., 2003]. Recent work has, however, suggested that the precipitation rates produced by ECHAM6 are more consistent with the best observational estimates of the surface energy budget, and that GPCP underreports precipitation [Kato et al., 2012; Stephens et al., 2012].

[63] In general, ECHAM6 inherits the structure of the precipitation biases of ECHAM5. The amplitude of the biases in ECHAM6 are slightly smaller than in ECHAM5, but can still be as large as  $5 \text{ mm d}^{-1}$  over broad regions in the tropics, and as much as  $2 \text{ mm d}^{-1}$  in the midlatitudes. High resolution, as shown in comparison with ECHAM5 in Figure 7 does little to ameliorate the problem. Biases in ECHAM can be characterized by a northward shift of the main Pacific basin precipitation features. These include the ITCZ, which is too poleward, and the South Pacific Convergence Zone that is shifted equatorward and is more

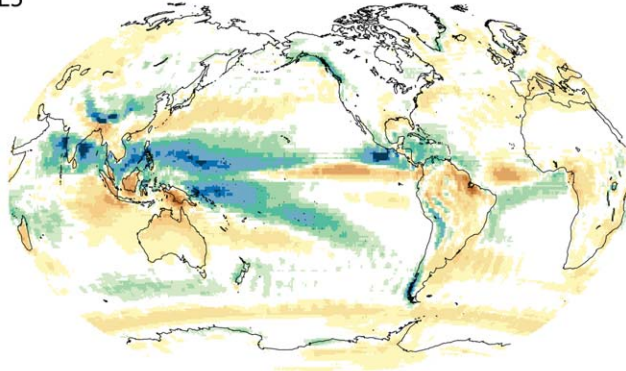


zonal than is observed. Even the Pacific storm-track in both hemispheres appears to be northward amplified. In the Atlantic too much precipitation falls south of the equator over the Atlantic and in the Caribbean, biases which may be related to the marked deficit of precipitation over tropical south America.

[64] The reasons why the amplitude of the ECHAM6 biases appear less pronounced than in ECHAM5 has not been studied in detail, but the prognostic variance used in the triggering of convection did, in the testing phase of the model, lead to better simulations of precipitation. Whether this difference is decisive, as for instance, compared to slight changes in tuning parameters that accompanied the final configuration of the model, is difficult to establish. Improvements in precipitation relative to earlier versions of ECHAM are more marginal, Figure 8, and seem to be little influenced by changes in resolution.

[65] There is also evidence that ECHAM6 precipitates too readily over extratropical continents and too little over tropical continents. This is shown with the help of Table 6, which compares various configurations of ECHAM6 with what is reported by GPCP. These issues

E5



HR

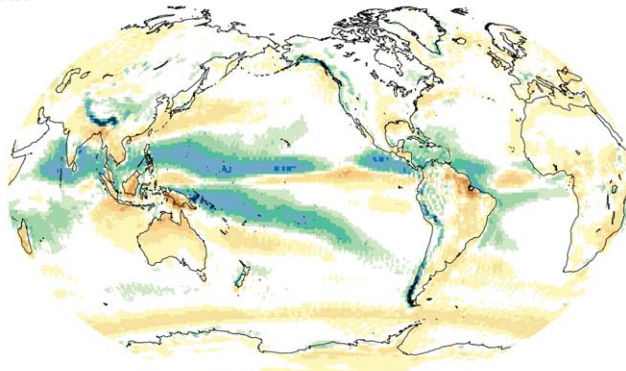


**Figure 7.** Difference in annual mean precipitation between ECHAM and GPCP (in units of  $\text{mm d}^{-1}$ ) for ECHAM5 (RMSE  $1.35 \text{ mm d}^{-1}$  upper), and the HR configuration of ECHAM6 ( $1.18 \text{ mm d}^{-1}$  lower).

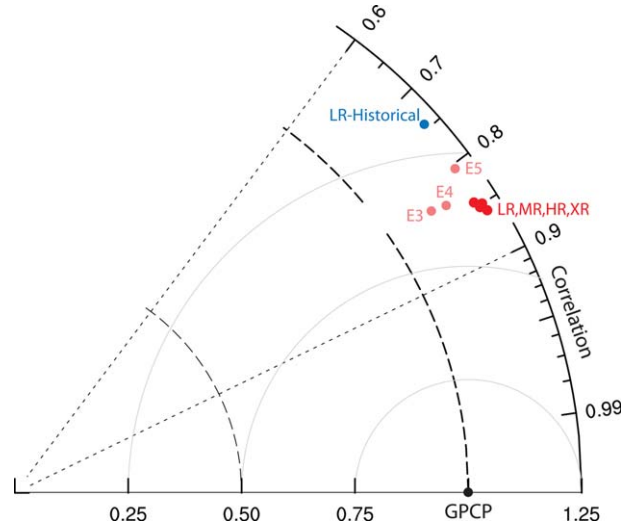


**Figure 8.** Taylor diagram of the annually averaged precipitation for various configurations of ECHAM with GPCP 1DD as the reference data.

are also explored in greater depth by T. Crueger et al. (Tropical precipitation and convection changes in the MPI-ESM in response to  $\text{CO}_2$  forcing, submitted to *Journal of Advances in Modeling Earth Systems*, 2012, hereinafter referred to as Crueger et al., submitted manuscript, 2012). In the GPCP record, the ratio of the average rain rate over the global land surface versus that over the global ocean is 0.71. In the different versions of ECHAM6 this ratio, falls to 0.63 for the LR model and 0.60 for the XR model. Between  $30^\circ\text{S}$  and  $30^\circ\text{N}$ , this relationship reverses in the observations as the ratio becomes 1.10, indicative of larger rain rates, on average, over land. Although it also increases in the model, this change is not as marked. LR has a tropical land-to-ocean rain-rate ratio of 0.91, which falls as resolution increases, to a value of 0.85 for the XR, coupling to the ocean does not lead to a marked change in this behavior. The precipitation rate over the global land surface varies between  $2.09$  and  $2.12 \text{ mm d}^{-1}$  similar to the  $2.14 \text{ mm d}^{-1}$  as reported by the GPCP; however, over the oceans the rain rate in the different configurations of ECHAM6 ranges from  $3.34$  to  $3.42 \text{ mm d}^{-1}$ , which is much larger than the  $2.85 \text{ mm d}^{-1}$  reported by the GPCP.

[66] Differences in the land-sea distribution of precipitation seem to depend on details, and are not robust across model versions. ECHAM4, which is similar to ECHAM3 in these respects, had on average larger rain

**Table 6.** Annually Averaged Precipitation (in Units of  $\text{mm d}^{-1}$ ) Subset by Subdomain for ECHAM

	GPCP	E4	E5	LR,MR, HR,XR	MPI-ESM-LR (Historical)
Global land	2.14	1.99	2.04	2.04–2.09	2.08
Global ocean	3.08	3.31	2.85	3.34–3.42	3.29
Tropical land	3.03	2.53	2.84	2.62–2.80	2.74
Tropical Ocean	2.78	2.99	2.59	3.01–3.08	2.97

rates over the tropical land surface than over the tropical ocean. *Mauritsen et al.* [2012] demonstrate that some improvement in the representation of precipitation over the maritime continent can also be attained by different parameter settings in the convective parameterization. Experiments (not shown) further indicate that the amount of precipitation over land is sensitive to the cloud radiative forcing, so that aspects of the precipitation problem may be coupled with aspects of the cloud problem. In the end, these differences are more indicative than decisive. The GPCP record is calibrated over the land, with the help of the surface rain-gauge network, but no such calibration is possible over the ocean, where independent measurements are scarce. Even so it seems unlikely that possible biases within the GPCP record can explain differences between what ECHAM6 simulates and what the GPCP reports.

#### 4.4. Tropical Variability

[67] ECHAM6 continues to have a good representation of tropical variability at a variety of timescales. This quality of the model has long distinguished it from many other state-of-the-art general circulation models [*Liess et al.*, 2004; *Sperber et al.*, 2005]. On intraseasonal timescales, research exploring factors influencing the representation of the Madden Julian oscillation (MJO) in ECHAM6 show that the changes Nordeng introduced into the deep convection scheme, which render it more sensitive to the humidity of the free troposphere, are largely responsible for ECHAM's ability to simulate MJO-like variability with some degree of fidelity [*Crueger et al.*, 2012]. Figure 9 shows the composite life cycle of the MJO as visualized by regressing on the principle component time series of the multivariate empirical orthogonal function (EOF) as described by *Waliser et al.* [2009]. By this and other measures, the simulation of the MJO in ECHAM is quite realistic, and suggests that a good simulation of intraseasonal variability in the tropics is possible with parameterized convection. This point is developed further by *Crueger et al.* [2012], who also show that the simulation of the MJO by ECHAM improves as resolution is increased, and when the atmosphere is coupled to the ocean.

[68] On interannual timescales, the most profound mode of tropical variability is associated with the El Niño-Southern Oscillation, or ENSO. ENSO variability in the MPI-ESM is improved relative to the ECHAM5/MPIOM (J. H. Jungclauss et al., Characteristics of the ocean circulation in the MPI-ESM CMIP5 experiments, submitted to *Journal of Advances in Modeling Earth Systems*, 2012), for which it was too strong. Observed large-scale shifts in precipitation associated with ENSO events are also well captured by ECHAM6. Figure 10 shows 30 years (1979–2008) of monthly precipitation anomalies from the Climate Prediction Center Merged Analysis of Precipitation (CMAP) data set [*Xie and Arkin*, 1997] regressed against monthly sea-surface temperature anomalies averaged over a box, Niño 3.4, which stretches from 5°S to 5°N and from 170°W to 120°W. AMIP simulations using ECHAM6 well represent the spatial pattern of precipitation changes that

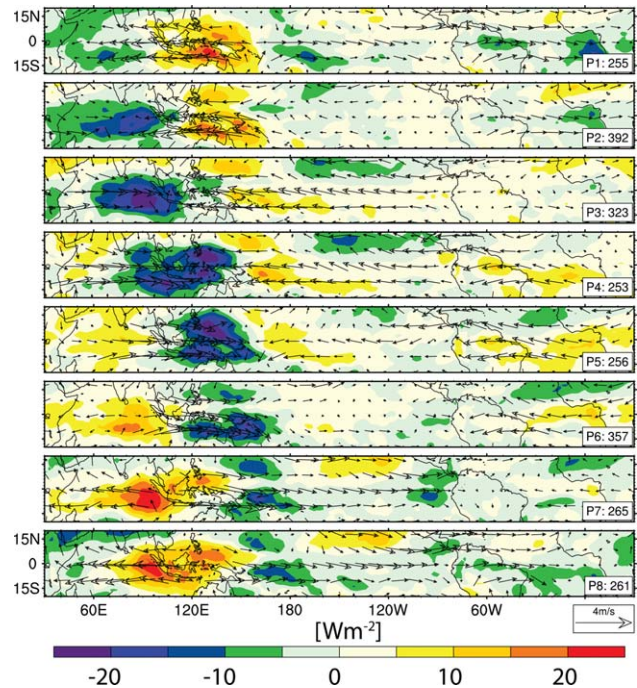


**Figure 9.** Madden Julian oscillation (MJO) lifecycle as represented in the MPI-ESM-HR. Nov–Apr 20–100-day filtered OLR (color) and 850 hPa wind anomalies regressed on the MJO index constructed from the square amplitude of the first two principle component time series derived from the multivariate EOF, following *Waliser et al.* [2009].

accompany the ENSO cycle, although the amplitude of the response in the model is somewhat larger than is observed.

[69] Given sufficient vertical grid spacing in the middle atmosphere, ECHAM6 is also able to represent the QBO as observed in the stratosphere and mesosphere. This is evident in Figure 11, where the zonally averaged zonal winds near the equator are shown to vary with a roughly 2 year periodicity and propagate downward similar to the observed QBO. There is some evidence that the QBO amplitude and frequency in the AMIP runs is too high. The QBO frequency becomes somewhat slower than observed in the coupled simulations. Because precipitation patterns are affected by coupling, this inference is consistent with the simulation of tropical precipitation playing a role in determining the structure of the QBO. The structure of the QBO is also sensitive to the choice of the parameters in the gravity wave parameterization, which through the course of tuning the model have been adjusted within limits to optimize the representation of the QBO. The semianual oscillation is also evident at higher altitudes. Further discussion of these issues is given in Schmidt et al. (submitted manuscript, 2012).

#### 4.5. Mean State and Circulation Features

[70] The mean thermal structure of the climate in ECHAM6 is slightly improved relative to previous



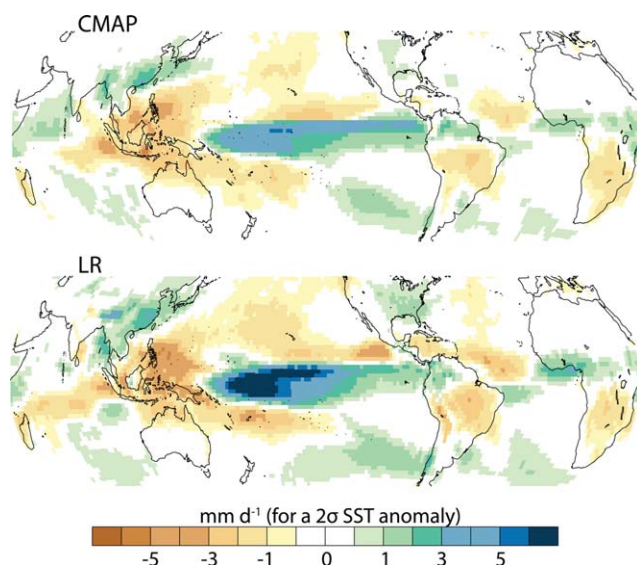


**Figure 10.** LR (AMIP) precipitation response to Equatorial SSTs derived by regressing monthly precipitation anomalies on Nino 3.4 SST anomalies (where anomalies are defined as difference from the mean) for a 30 year, 1979–2008, period. For the purpose of illustration, the regression coefficient is multiplied by twice the standard deviation of the SST anomaly, 2.56 K, to derive the precipitation anomaly.

versions of ECHAM, although not in every respect. The most marked improvement is in the lower stratosphere in the extratropics, where the cold biases in both the summer and winter hemisphere are significantly reduced. This is illustrated in Figure 12 for the boreal winter season, but boreal summer shows similar improvements. There is some evidence that these improvements might benefit from the higher model top, and improved vertical resolution in the tropopause region, which would be consistent with the further improvement evident in the MR, relative to the LR model. Although the extratropical stratospheric temperature is better represented, the upper tropical troposphere has slightly larger, 1 K, cold biases in ECHAM6 as compared to ECHAM5. Other biases remain largely unchanged. The hint of a surface-confined cold bias is apparent over Antarctica in its summer season and a warm bias is apparent in the lower to mid-troposphere over the Arctic. The latter is most evident in the AMIP simulations and can presumably be attributed to the specification of rather thin winter ice. The tropics and mid-latitudes of the summer hemisphere are also somewhat less stably stratified in ECHAM than they are in the reanalysis, with a slight warm bias in the lower troposphere below 800 hPa and a cold bias above.

[71] To explore the effect of resolution on temperature and other biases, experiments with an enhanced vertical resolution configuration of the XR model were performed. In this enhanced version, 199 levels were used, instead of the standard 95 levels. Most of the additional levels were concentrated in the troposphere and stratosphere where the vertical resolution

was kept to 300 m or less. This configuration of the model required large damping in the upper atmosphere, and required very short computational time steps to run stably, which further compounded the computational cost of this model. The computational cost of the model meant that there was little opportunity to adequately tune it, and as a rule, this configuration more poorly simulated the overall climate. Among the exceptions to this rule was the thermal structure of the atmosphere in the upper troposphere and lower stratosphere in which biases were significantly reduced (not shown). And although the reduction of temperature biases in the upper tropical troposphere may have resulted from differences in the behavior of the convection scheme at such high resolution, it appears likely that reduced vertical mixing from numerical diffusion may have played a role, particularly in the extratropics. Enhanced resolution has, however, very little effect on the temperature biases in the lower troposphere, e.g., Figure 12.

[72] An improved representation of the zonally averaged circulation in ECHAM6 accompanies the slight improvements in the zonally averaged thermal structure of the atmosphere. Here analysis focuses on the MR configuration, because it has slightly smaller temperature biases (Figure 12) and the improvements as compared to ECHAM5 are more readily apparent. Although the biases in ECHAM6 have a similar structure to the biases in ECHAM5, they are much weaker in amplitude, as shown in Figure 13. The pattern of the zonally averaged biases can be characterized by the tendency of the westerlies in the mid-latitudes to be insufficiently poleward, and the circulation associated with the first baroclinic mode in the tropics to be too strong. The biases in the mid-latitudes are evident in both hemispheres, but are more dominant in the southern hemisphere. Figure 13 further demonstrates that within a hemisphere the bias in the westerlies is more pronounced in the summer season of that hemisphere, but this is also where the improvement in the MR configuration of ECHAM6 over ECHAM5 is most apparent. Biases in the tropics are characterized by low level easterlies that are too strong and upper levels that are

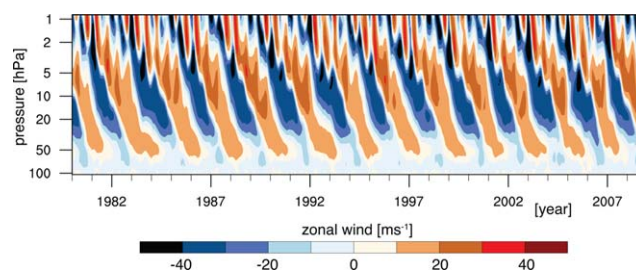


**Figure 11.** Stratospheric variability. Shown are the amplitude of the zonal winds as a function of pressure and time in the middle atmosphere (above 100 hPa). The winds are averaged over the tropical belt, between 5°S and 5°N and are taken from the AMIP run of the MR model.



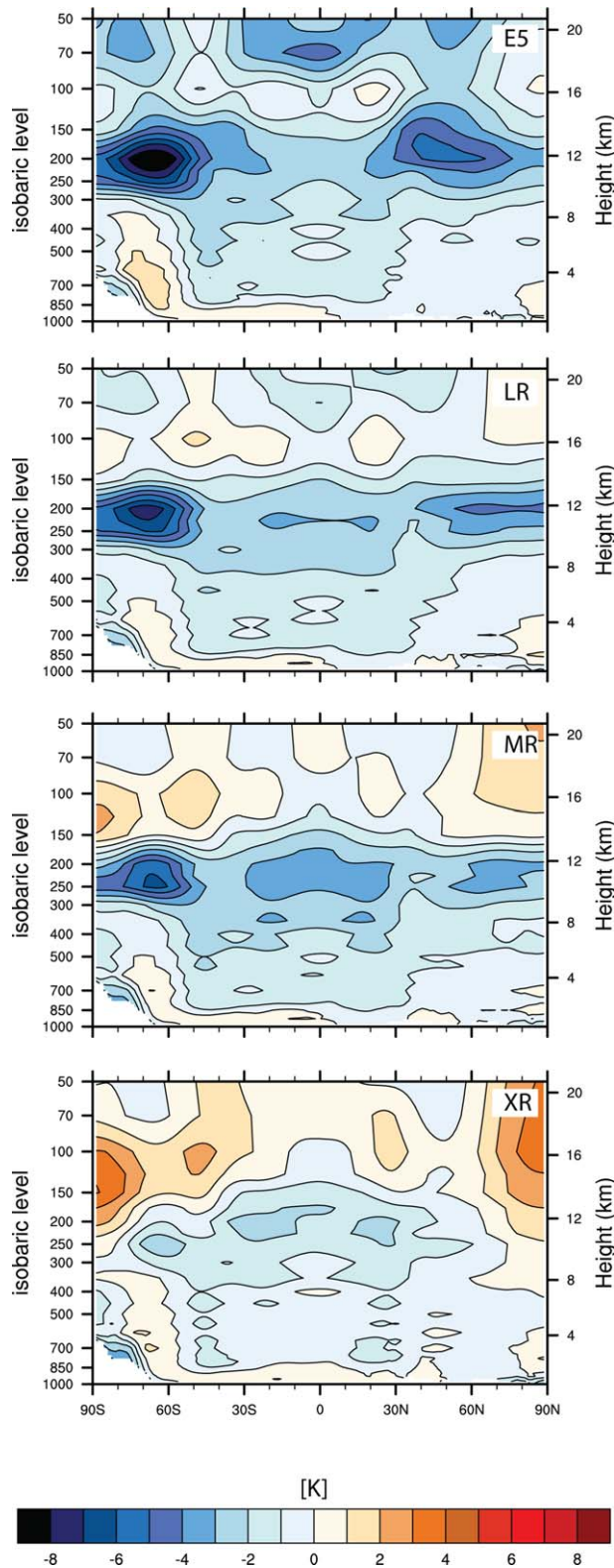


**Figure 12.** Differences between simulated and reanalysis (ERA-Interim) temperatures zonally averaged for the boreal winter (DJF) in the troposphere and lower stratosphere.

more westerly than in the reanalysis, suggestive of too much heating by deep convection.

[73] The stationary wave structure is also improved in ECHAM6. This is evident in Figure 14, which compares the solstice season sea-level pressure biases relative to the ERA-Interim reanalysis [Dee *et al.*, 2011] for ECHAM5, and for the LR and HR configurations of ECHAM6. Only in the north Atlantic region during winter is there an evidence of deterioration of the stationary wave pattern. When viewed from the perspective of the 500 hPa geopotential height anomalies, this bias is associated with a slight westward shift in the troughs centered over eastern Europe and off the east coast of north America, and more zonal flow over the Atlantic in the HR model. These differences might explain why the HR model drives a weaker meridional overturning circulation in the Atlantic and performs less successfully when coupled to the ocean model. The hemispheric low-level temperature bias (Figure 12), wherein the simulated temperature differences between the south and north polar regions is larger than what is observed, may also contribute to a weaker Atlantic overturning circulation.

[74] During the tuning process, the model development team used a summary of the circulation features, as measured by a simple version of the performance index introduced by Reichler and Kim [2008], as input into their decision making process. The variables contributing to the performance index are summarized in Table 7. Following Reichler and Kim [2008], only the annual climatology was taken into consideration, weighted by the interannual variance of a given field, and the relative error as compared to the CMIP3 ensemble of 20 models for which complete data are available. Each simulated field was interpolated from its native grid to the native grid of the observational data set used as a reference. A performance index of unity denotes the average performance of a CMIP3 model, and values less than unity denote improved performance relative to an average CMIP3 model. Mauritsen *et al.* [2012] describe how different fields contribute to the indices and show that different configurations of ECHAM6 (which is to be expected given the advantage of specified sea-surface temperatures), as well as the MPI-ESM, outperform the average CMIP3 model in almost every respect. Only in the representation of precipitation can ECHAM6 be considered about, albeit a bit better than, average.

[75] The modified performance index measures the improvements in the representation of the mean climate by ECHAM6 relative to ECHAM5, and more broadly relative to earlier generations of ECHAM, e.g., Figure 15. These improvements are most evident when the model is run in an uncoupled mode, and the HR model outperforms all others in this mode. For the coupled simulations, the LR model still represents a substantial improvement, 0.50 as compared to 0.56 for ECHAM5, with most of the improvement manifest in the extratropical circulation. While this might reflect slightly better luck with the tuning, we suspect that the higher model top and improved resolution in the upper

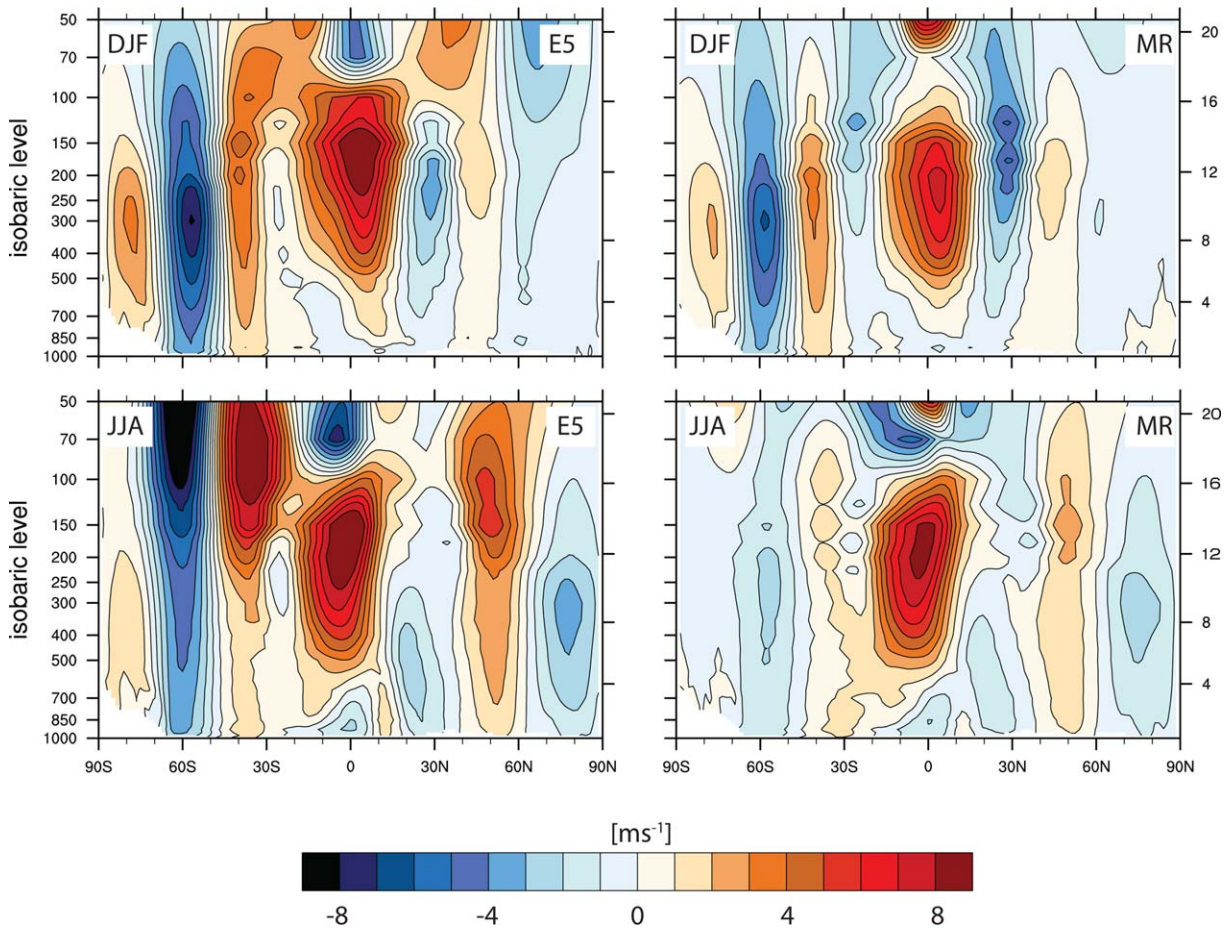


**Figure 13.** Differences between simulated (ECHAM5 and MR) and reanalysis (ERA-Interim) zonal winds, zonally averaged for the boreal winter (DJF) and boreal summer (JJA) seasons.

troposphere and lower stratosphere to be the more critical factor. Modifications to the radiation and surface albedo would be expected to more strongly affect the tropical circulation for which only the fixed SST versions show improvement. SST biases, such as a too strong equatorial Pacific cold tongue, that emerge only when the atmosphere and ocean are coupled (e.g., Giorgetta et al., submitted manuscript, 2012), dominate the biases in the tropics in the coupled model. As measured by this performance index, ECHAM6 provides a better representation of the mean climate than did ECHAM5, where ECHAM5 was already among the best performing CMIP3 models. This conclusion is further supported by the analysis of Anav et al. [2012] who ranked the MPI-M-LR highest within a group of 17 CMIP5 models in terms of its representation of surface temperature and precipitation.

## 5. Climate Sensitivity and Forcing

[76] In this section, basic features of the response of ECHAM6 to a quadrupling of  $\text{CO}_2$  concentrations are outlined. Traditionally the equilibrium climate sensitivity is defined as the change in the surface temperature,

produced by an atmospheric model coupled to a slab ocean, in response to a doubling of the atmospheric  $\text{CO}_2$  concentration. As such it can be viewed as an intrinsic property of the atmosphere, which motivates our interest in this quantity in our overview of the atmospheric component of the MPI-ESM. However, because the CMIP protocol did not include slab ocean experiments, the equilibrium climate sensitivity of ECHAM6 must be evaluated from simulations of the full ESM.

[77] The response to increasing  $\text{CO}_2$  concentrations can be broken down into two components. A fast response associated with the changing concentrations of  $\text{CO}_2$  and the net response, which includes the effect of the gradually warming ocean that slowly adjusts to the surface energy imbalance associated with changing  $\text{CO}_2$  concentrations. This breakdown is informative because the fast response is amenable to investigation by very high-resolution models, which are too computationally expensive to study slower feedback processes (cf., Wyant et al. [2012] and S. Bony et al., Direct effect of carbon dioxide on tropical atmospheric circulation and regional rainfall, submitted to *Nature Geoscience*, 2012, hereinafter referred to as Bony et al., submitted



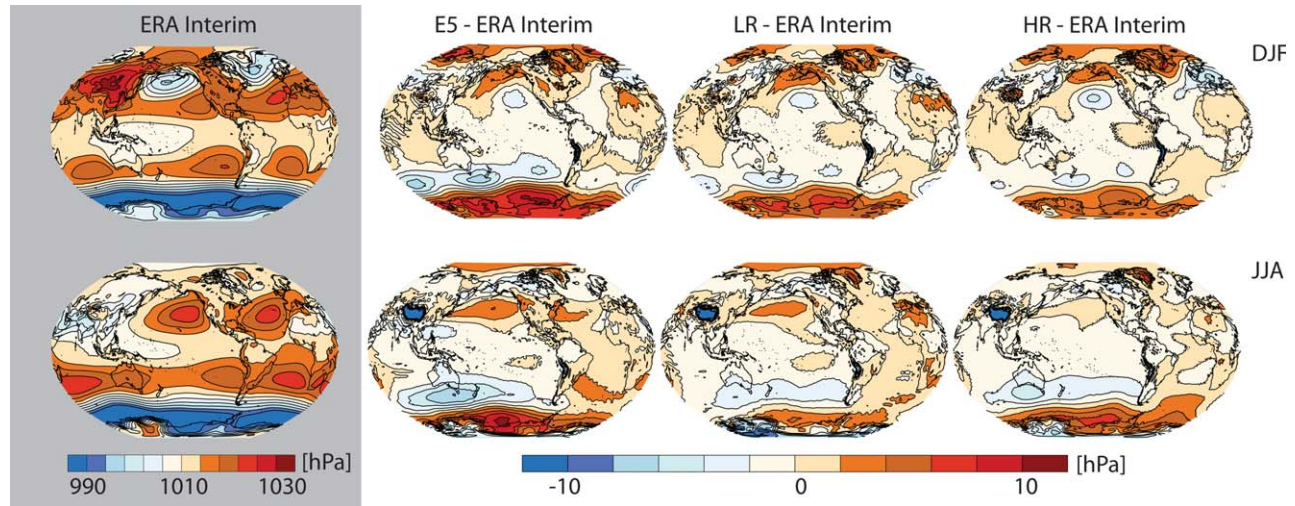


**Figure 14.** Mean sea-level pressure. (left) The climatology of the ERA-Interim is shown. (right) Differences relative to the reanalysis (ERA-Interim) for three different versions of ECHAM: ECHAM5, and the LR and HR configurations of ECHAM6.

manuscript, 2012). The fast response to an abrupt increase in atmospheric  $\text{CO}_2$  concentrations can be measured by computing the changing surface temperatures and patterns of precipitation that accompany an increase of  $\text{CO}_2$  with sea-surface temperatures held fixed. This response is illustrated in Figure 16 and is characterized by local, approaching 3 K, warming over the continents. The response is stronger in the northern hemisphere where the landmasses are larger. The precipitation anomalies, particularly the increase over tropical land-surfaces (most evident in Figure 16 over Australia, Africa, and the maritime continent) are consistent with this pattern of warming, drives more convergence over land, and that this is accompanied by more precipitation. The interpretation is that the

enhanced surface temperatures over land, which expresses the smaller effective heat capacity of the land surface. Although the ocean temperatures are held fixed in these experiments, in a coupled simulation the first years would see little warming of the ocean; running with a fixed SST mainly improves the sampling of the fast response that would also occur if SSTs were allowed to freely evolve. It follows that precipitation over the tropical oceans is, through this same process, suppressed; although as discussed by Bony et al. (submitted manuscript, 2012) a reduction of precipitation over the ocean is also evident in aquaplanet simulations because the change in the atmospheric cooling profile associated with increased  $\text{CO}_2$  leads to a more stably stratified atmosphere.

[78] The response to a quadrupling of atmospheric  $\text{CO}_2$ , as measured by the difference between the piControl and the last 30 years of the abrupt4 $\times\text{CO}_2$  simulations of the MPI-ESM (i.e., the coupled model) is characterized by pronounced warming over the Arctic, similar to the familiar pattern of warming from atmosphere models coupled to slab ocean models [Randall et al., 2007]. The relatively small changes in temperatures over the Southern Ocean and north Atlantic are likely not characteristic of the final response; after 150 years of integration the deep ocean is still very far from equilibrium. Very long integrations with ECHAM5 coupled to the MPIOM show that as the deep ocean comes into equilibrium the asymmetry between the poles is somewhat reduced [Li et al., 2012]. Warming over the continents by the end of a 150 year period simulated by the abrupt4 $\times\text{CO}_2$  experiment have land temperatures which are elevated by 6–8 K and even more in the far north. The broad outline of changes in precipitation, for instance the zonal mean structure, is characteristic of what one would expect from simple thermodynamic arguments [e.g., Held and Soden, 2006], wherein changes to the absolute humidity coupled to the pre-existing

**Table 7.** Variables Contributing to the ECHAM Performance Index<sup>a</sup>

Quantity	Domain	Data Source
Precipitation	Global	CMAP, GPCP
Precipitable water	Global	HOAPS, NVAP
Sea-level pressure	Global	ICODS, HadSLP2, ERSLP
Surface-air temperature	Global	CRU, NOAA, ICOADS
Stationary waves 500 hPa	Global	ERA-40
Geopotential 500 hPa	Global	ERA-40
Temperature 850 hPa	Global	ERA-40
Zonal surface wind stress	Ocean	ICODS, GSSTF2
Meridional surface wind stress	Ocean	COADS, GSSTF2
Sea ice cover	Ocean	GISST
Temperature	Zonal mean	ERA-40
Zonal wind	Zonal mean	ERA-40

<sup>a</sup>Note that for the simulations with fixed SSTs the surface-air temperature is strongly constrained by the specified sea-surface temperature, and the sea-ice cover is prescribed.



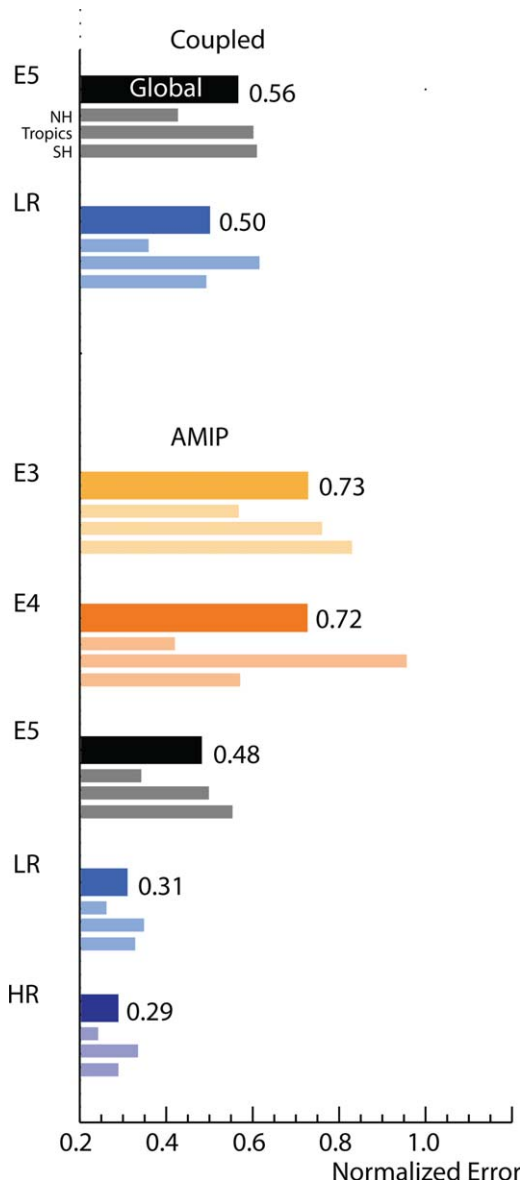


**Figure 15.** Modified Reichler-Kim standardized error based on analysis fields summarized in Figure 7. A value of one denotes the average of the CMIP3 models.

circulation will increase the moisture convergence in the regions where there is already moisture convergence and rainfall, and increase the moisture divergence from those regions where there is pre-existing moisture divergence, thus making them drier. This is evident in the increase of precipitation in the Pacific ITCZ regions, Figure 17, and in the storm tracks, and the decrease in precipitation in subsidence zones of the subtropics. Some regions (e.g., tropical South America, and the tropical Atlantic south of the equator) depart markedly from what would be expected from a simple wet-get-wetter type of argument, suggesting that dynamical processes [Chou and Neelin, 2004; Chou et al., 2009] likely are playing an important role. Although the effect of the fast response of precipitation to changing atmospheric  $\text{CO}_2$  concentrations is still evident, in that as a

rule more rain falls over tropical land, the pronounced drying over the Amazon, Figure 17, also stands out as the exception to this rule. Because the model exaggerates the precipitation response to regional temperature changes, as for example evidenced by regressed precipitation versus Nino 3.4 temperature anomalies in the present climate, Figure 10, and because it underestimates precipitation over tropical land in general, and the Amazon in particular (Figure 7), the authors are hesitant to attach much weight to this feature.

### 5.1. Regression Analysis of Global Changes

[79] The analysis framework introduced by Gregory et al. [2004] provides a useful framework for summarizing, and quantifying, the global response of ECHAM6 to a change in the radiative forcing. By regressing the irradiance imbalance at the top of the atmosphere against changes in surface temperature, it is possible to identify an adjusted (radiative) forcing and a climate sensitivity that accompanies the imposed perturbation.

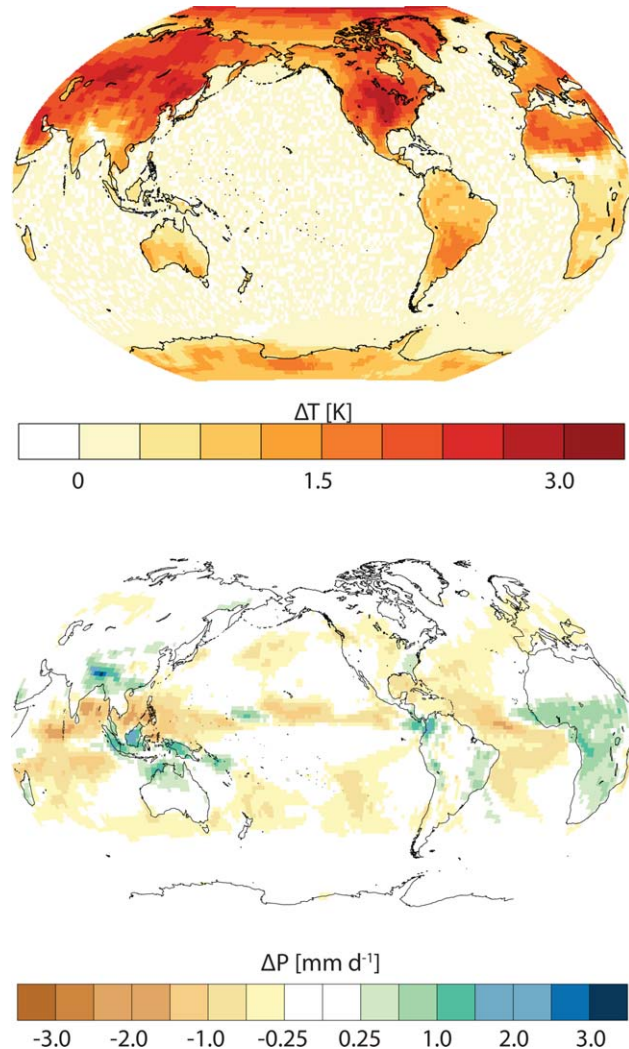


**Figure 16.** Difference in (top) surface temperature and (bottom) precipitation between the last 30 years of the climSST4 $\times$ CO $_2$  and the climSST simulations.

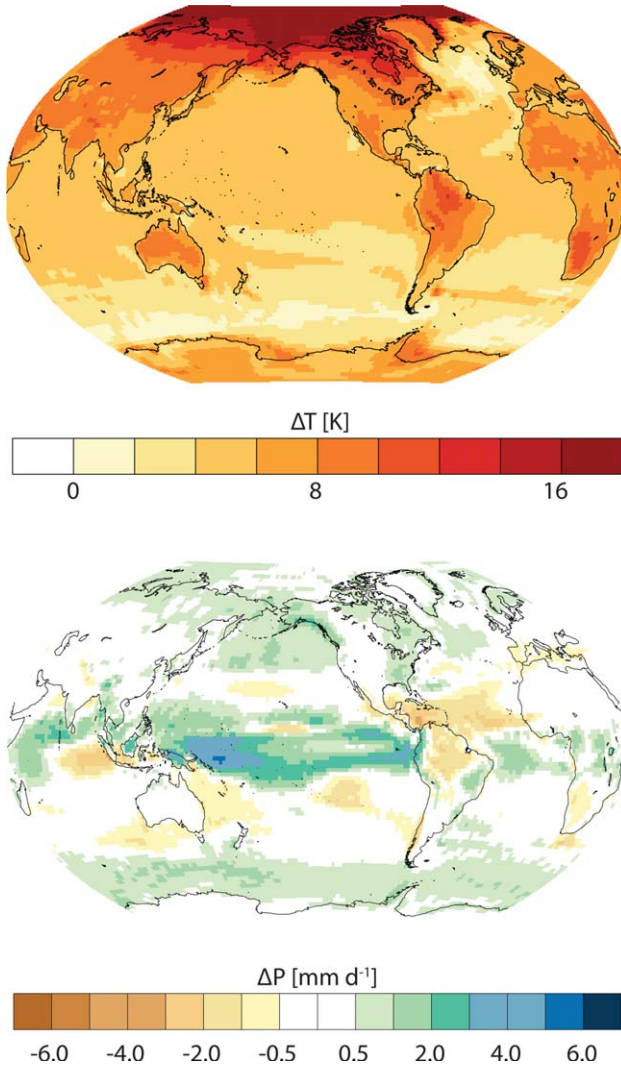


**Figure 17.** (top) Difference in surface temperature and (bottom) precipitation between the last 30 years of the abrupt4×CO<sub>2</sub> and the mean of the piControl simulations. Note the more than a factor of 5 change in the temperature scale and the factor of 2 change in precipitation as compared to Figure 16.

Based on this analysis we estimate an adjusted forcing of  $4.09 \text{ W m}^{-2}$  for a doubling of atmospheric CO<sub>2</sub> concentrations, and a climate sensitivity of 2.9–3.4 K, Figure 18. The climate sensitivity is somewhat larger, although the adjusted forcing is somewhat smaller for the LR model, with numeric values being provided in Table 8.

[80] There are two methodological issues that introduce considerable uncertainty into estimates of the climate sensitivity (as defined above) and the adjusted forcing. To begin with the regression is usually performed by associating degrees of freedom in the temperature response with time intervals in a simulation that is adjusting to a change in the atmospheric CO<sub>2</sub> concentration. Doing so inordinately weights the response of the system near the new equilibrium, as the model

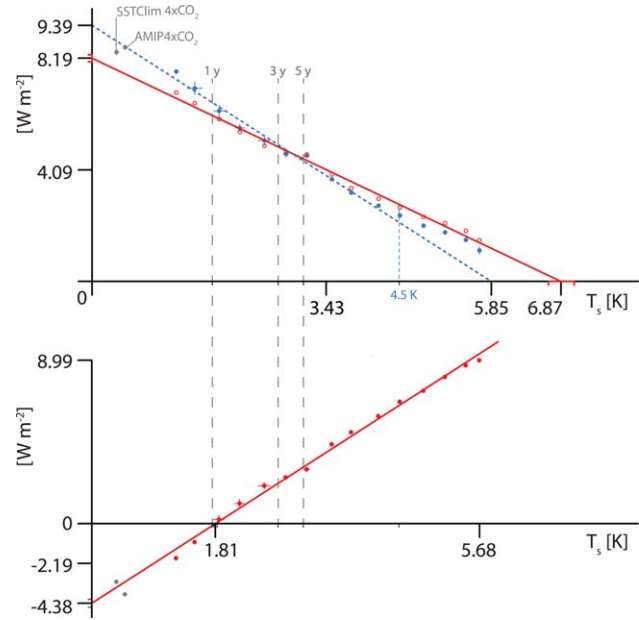


**Figure 18.** (top) Gregory-like analysis of climate sensitivity and adjusted radiative forcing and (bottom) change in surface evaporation for the MR Configuration. (top) Blue markers are for the TOA net irradiance (abrupt - piControl) with dotted regression line based on points with a temperature increase less than or equal to 4.5 K. Uncertainty is denoted by bars with plus or minus twice the standard error from estimates that fall within the indicated temperature range. Gray markers show response of AMIP4×CO<sub>2</sub> and climSST4×CO<sub>2</sub> simulations relative to base AMIP and climSST simulations. Red points and red regression are for the surface energy budget. (bottom) Changes in surface evaporation are shown as a function of temperature change, gray points are from the AMIP and ClimSST simulations.

spends most of its time there. We instead bin temperature data in 0.25 K intervals and base our regression on single data points within each temperature interval, which leads to a more robust regression estimate, but one that can differ from more traditional estimates, as for instance, as given in the summary paper by Andrews *et al.* [2012]. The second issue is more crucial, and may be an artifact of the lack of energy conservation in ECHAM6. All versions of ECHAM have had small

**Table 8.** Forcing and Sensitivity of the MR and LR Models to a Quadrupling of Atmospheric CO<sub>2</sub><sup>a</sup>

Quantity	MR	LR
y intercept (Sfc) ( $\text{W m}^{-2}$ )	8.18	8.07
y intercept (TOA) ( $\text{W m}^{-2}$ )	9.39	8.95
y intercept (clear sky TOA) ( $\text{W m}^{-2}$ )	10.89	10.65
x intercept (TOA) (K)	5.85	6.52
x intercept(Sfc) (K)	6.87	7.42

<sup>a</sup>For reference, Andrews *et al.* [2012] estimates the adjusted forcing at TOA to be  $8.18 \text{ W m}^{-2}$  and the x intercept to be 7.26 for the LR simulations.

inconsistencies in the energy budget, for instance, through the inconsistent treatment of moisture contributions to the specific enthalpy, which lead to a few tenths of a watt per square meter offset in the TOA in equilibrium. Recent experience during the CMIP5 exercise have, however, shown these biases to be temperature dependent, which inherently biases Gregory like estimates, as the energy offset at the new equilibrium will not equal the energy offset at the old equilibrium. Although the former is known from the long-term pre-industrial control experiments, the latter is not known until the system reaches stationarity, which for coupled systems can take thousands of years.

[81] One way to avoid possible artifacts introduced by lack of energy conservation is to examine the surface energy balance, as is illustrated by the red points in Figure 18 and tabulated in Table 8, and for which the energy leakage is effectively zero. The disadvantage of the surface energy budget is that the disequilibrium between the atmosphere and ocean may depend on how hard the system is driven, and hence relax over time, which would be reflected as a slight difference in the slope of the regression based on the surface energy budget as compared to the energy budget at the TOA. These differences, perhaps compounded by the effects of the energy leakage, conspire so that the surface energy budget regression better fits the data over the full range of the temperature response, whereas the TOA response shows differentiated behavior, a kink, with the slope of the imbalance in the TOA irradiance, versus temperature, flattening at temperatures changes larger than about 4.5 K. Although this would suggest that the kink may, at least in part, result from the lack of energy conservation in ECHAM6, independent analysis raises the possibility that this is a physical response of the system (K. Block and T. Mauritsen, Forcing and feedbacks in ECHAM6, submitted to *Journal of Advances in Modeling Earth Systems*, 2012, hereinafter referred to as Block and Mauritsen, submitted manuscript, 2012), in which case the lack of such a feature in the surface energy budget analysis would be fortuitous. In any case, these issues introduce an uncertainty in the estimate of the climate sensitive of about 15% and explain the range of 2.9–3.4 K that is estimated for the MR configuration of ECHAM6.

[82] The precipitation response to warming is shown in Figure 18 (bottom). Here the composition of the precipitation response in terms of a fast response, or adjustment, that is characterized by a reduction in precipitation, followed by a slow increase in precipitation, with a slope of  $2.35 \text{ mm d}^{-1} \text{ K}^{-1}$  is readily evident. An abrupt increase in atmospheric  $\text{CO}_2$  concentrations stabilizes the atmosphere and reduces precipitation overall, see also Figure 16, but is compensated for by the tendency of the precipitation to increase again as the system warms. In these respects, ECHAM6 behaves similarly to other models, as documented by Bony et al. (submitted manuscript, 2012).

[83] Both cloud feedbacks and the (fast) cloud adjustment in ECHAM6 act to amplify the warming from increasing greenhouse gas concentrations. The feedback

mechanisms are analyzed in more detail using a combination of the Gregory and Kernel methods, as described by Block and Mauritsen (submitted manuscript, 2012). Here this analysis is used to show the contribution to the warming from fast cloud adjustments and feedback, where the latter is measured by the cloud feedback parameter whose units are  $\text{W m}^{-2} \text{ K}^{-1}$ . Over most of the globe, both the cloud adjustment is positive, which indicates that clouds adjust to changes in radiative forcing so as to amplify the forcing. The responses, which are relatively similar across a wide variety of cloud regimes, presumably arise for different reasons, but combine to give a cloud adjustment of  $1.6 \text{ W m}^{-2}$  on the global average. The response pattern is zero or positive almost everywhere, the exception being the mid-latitude storm tracks, whose adjustment works to reduce the forcing, Figure 19. The cloud feedback parameter is also positive over most of the globe with a globally averaged value of  $0.6 \text{ W m}^{-2} \text{ K}^{-1}$ . In regions of deep convection the longwave effect from raising cloud top heights, as documented by Crueger et al. (submitted manuscript, 2012) dominates the response. Over the subtropical oceans, there appears to be a robust reduction in low-level cloudiness, which through its effect on the shortwave radiative budget also amplifies the forcing.

## 6. Summary

[84] This paper describes ECHAM6, the sixth generation of the atmospheric general circulation model ECHAM. ECHAM6 forms the atmospheric component of the MPI-ESM, a coupled climate model that includes dynamic vegetation, and interactive carbon cycle, as well as advanced representations of atmosphere and ocean processes. Previous generations of ECHAM have been thoroughly described in a series of technical reports, but because these reports are increasingly difficult to access, and can be difficult to cite, in this paper, additional emphasis has been placed on documenting the basic features of ECHAM6, rather than just the changes relative to the previous generation of ECHAM, ECHAM5.

[85] In comparison to ECHAM5, the main changes implemented in ECHAM6 have to do with the treatment of shortwave radiative transfer, the development of a new surface albedo representation, a new aerosol climatology, and ongoing efforts to add complexity to the representation of the land surface, for instance, through the inclusion of dynamic vegetation. ECHAM6 has been developed to run across a wide-range of horizontal resolutions, ranging from the very coarse (T31) to experimental studies at T255. The T31 model has 31 levels, and has a low (10 hPa) model top. It has been tuned for instructional purposes, and lends itself well to applications that do not depend heavily on a well resolved atmospheric circulation. In general, the higher resolution models perform slightly better, but for the resolutions of T63 or higher, which have been the focus of the present analysis, the limiting factor in model performance appears to be primarily the physical



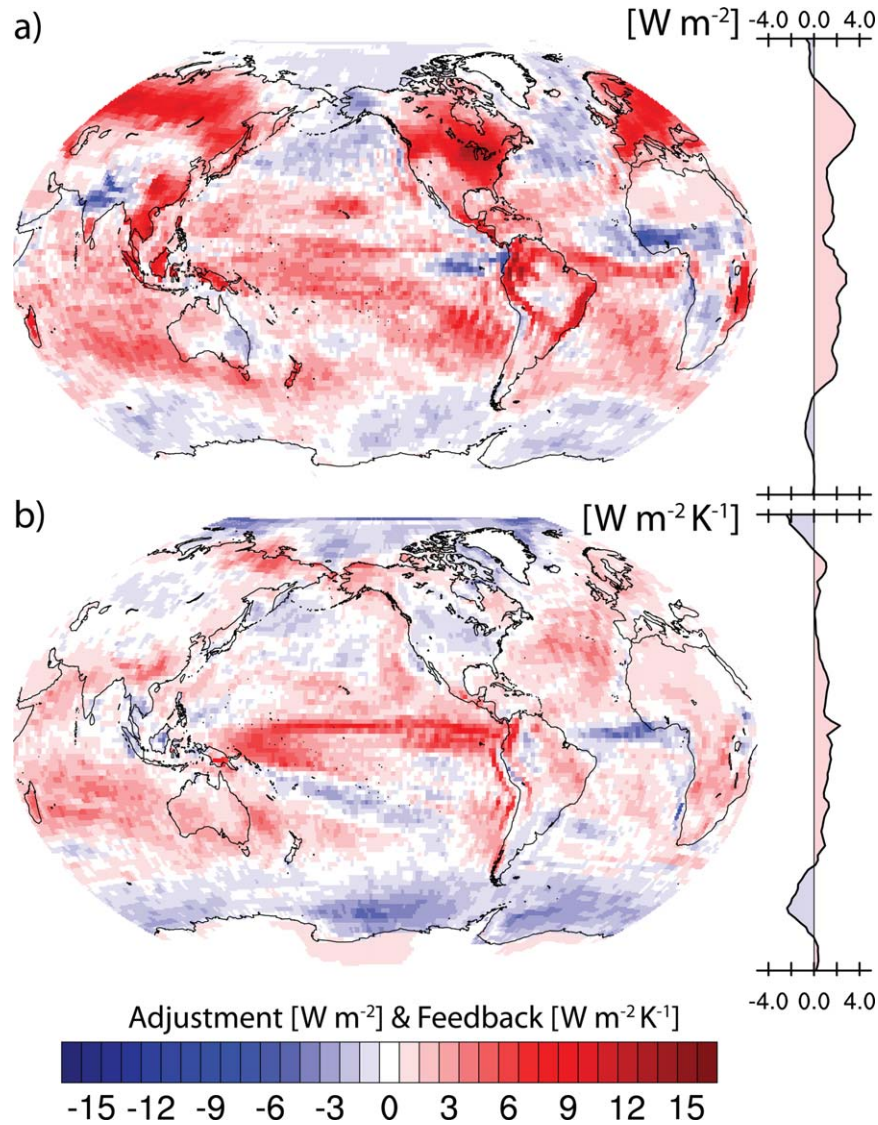


**Figure 19.** (top) The contribution of clouds to the adjusted forcing measures the contribution to the radiative forcing from cloud adjustments (or fast responses) to changing  $\text{CO}_2$  concentrations. (bottom) Cloud feedback parameter measure the change in cloudiness that correlates with changes in surface temperature. Analysis is performed for the LR model. The globally averaged adjustment and cloud feedback are  $1.6 \text{ W m}^{-2}$  and  $1.6 \text{ W m}^{-2} \text{K}^{-1}$ , respectively.

parameterizations. Except for the coarse, T31 configuration, all configurations are based on either a 47 or 95 level vertical grid, with the top model level centered at 0.01 hPa, thereby subsuming the middle-atmosphere development branch that had been developed alongside ECHAM4 and ECHAM5. The 47 and 95 level configurations of ECHAM6 differ in their resolution of the upper troposphere and lower stratosphere. Minor changes have also been introduced into ECHAM6 through changes to the convective triggering, and different choices of tuning parameters. The tuning strategy has been partly described in the present manuscript, but is more extensively described in an accompanying publication [Mauritsen et al., 2012].

[86] ECHAM6 better simulates many aspects of the present climate as compared to ECHAM5. The greatest improvements are in the mid-latitudes. Although improvements in the tropical circulation, including tropical precipitation, are evident when the model is uncoupled, coupling degrades the simulation so that ECHAM6 only marginally improves upon ECHAM5 in the tropics when coupled to an ocean model. ECHAM6 has a particularly satisfactory representation of tropical variability, including a robust representation of tropical intraseasonal variability, the QBO in the middle atmosphere, and the response of precipitation to changes in sea-surface temperatures over the equatorial Pacific, as for instance accompany El Niño.

[87] No systematic deterioration in the representation of the current climate, relative to what was simulated by ECHAM5, has been identified. Nonetheless a number of stubborn biases endure. Overall there has been relatively little improvement in the representation of precipitation since the introduction of ECHAM3, the oldest version of ECHAM whose simulations are still accessible. Precipitation over land is too weak, and there is a global tendency of precipitation features, from the South Pacific Convergence Zone to precipitation over the Gulf Stream, to be shifted too far northward. Biases in the representation of marine boundary layer clouds remain large, with such cloud layers appearing too infrequently in the simulations, but being too bright when they do appear. ECHAM6 continues to have large (3 K) cold biases in upper tropospheric temperatures, with a hint of improvement relative to ECHAM5 in the extra-tropics. Tropical temperature biases only vanish with very high (300 m) vertical resolution in the upper troposphere. The tropical and mid-latitude convective stability of the troposphere remains more unstable relative to observations, particularly in the southern hemisphere in its summer season. The extratropical jets maximize at somewhat lower latitudes than observed (see also *Kidston and Gerber* [2010] who document similar biases in the family of CMIP3 models), particularly in the southern hemisphere during austral summer.

[88] The model response to increasing concentrations of atmospheric CO<sub>2</sub> is within the mid-range of estimates of other comprehensive GCMs, and is amplified by cloud processes. Aerosol radiative interactions play a relatively minor role, contributing a forcing of 0.34 W m<sup>-2</sup>. Aerosol cloud interactions are represented in a time-invariant fashion, as it is assumed that these myriad and complex effects largely compensate one another, and thus do not contribute meaningfully to the adjusted forcing. An evaluation of this assumption is not possible given present understanding of the interplay between cloud micro and macrophysical processes. Clouds tend to amplify the warming associated with a quadrupling of atmospheric CO<sub>2</sub>, both on short timescales where they adjust directly to changes in CO<sub>2</sub> concentrations so as to increase the radiative forcing, and on longer timescales where they change in response to increasing sea-surface temperatures, and can be thought of as a feedback on the radiative forcing. The main cloud feedbacks arise in the tropics, in association with the deepening of the tropical troposphere, which is reasonably well understood, and in the subtropics, where boundary layer clouds are reduced as the surface temperatures warm, but for reasons that remain unclear.

[89] **Acknowledgments.** B.S. would like to acknowledge the seminal contributions of Erich Roeckner (now retired) to the development of this and every version of ECHAM before it. ECHAM6 is the culmination of three decades of model development led and motivated by E.R. To the extent that ECHAM6 represents the general circulation of the atmosphere with any fidelity is a testament to his scientific vision, his passion, and those of an evolving team of kindred spirits whose efforts E.R. helped organize. The Max Planck Society for the Advancement of Science is thanked for their support of this research. The research leading to these results has also received funding from the European Union, Seventh Framework Programme (FP7/2007-

2013) under grant agreement 244067. The XR simulations were made possible by the STORM consortium, and funding by CliSAP, an excellence cluster at the University of Hamburg supported by the German Science Foundation. Computational resources were made available by Deutsches Klimarechenzentrum (DKRZ) through support from the Bundesministerium für Bildung und Forschung (BMBF).

## References

- Adler, R. F., et al. (2003), The version 2 global precipitation climatology project (GPCP) monthly precipitation analysis (1979-present), *J. Hydrometeorol.*, **4**(6), 1147–1167.
- Anav, A., et al. (2012), Evaluating the carbon cycle components of CMIP5 EARTH SYSTEM MODELS, *J. Clim.*, in press.
- Andrews, T., J. M. Gregory, M. J. Webb, and K. E. Taylor (2012), Forcing, feedbacks and climate sensitivity in CMIP5 coupled atmosphere-ocean climate models, *Geophys. Res. Lett.*, **39**, L09712, doi:10.1029/2012GL051607.
- Baines, P. G., and T. N. Palmer (1990), Rationale for a new physically-based parameterization of subgridscale orographic effects, *Tech. Rep. 169*, ECMWF, Reading, U. K.
- Bengtsson, L., K. I. Hodges, M. Esch, N. Keenlyside, L. Kornbluh, J.-J. Luo, and T. Yamagata (2007), How may tropical cyclones change in a warmer climate? *Tellus A*, **59**(4), 539–561.
- Bodas-Salcedo, A., et al. (2011), COSP: Satellite simulation software for model assessment, *Bull. Am. Meteorol. Soc.*, **92**(8), 1023–1043.
- Brinkop, S., and E. Roeckner (1995), Sensitivity of a general circulation model to parameterizations of cloud-turbulence interactions in the atmospheric boundary layer, *Tellus A*, **47**(2), 197–220.
- Brovin, V., T. Raddatz, C. Reick, M. Claussen, and V. Gayler (2009), Global biogeophysical interactions between forest and climate, *Geophys. Res. Lett.*, **36**(7), L07405, doi:10.1029/2009GL037543.
- Cheper, H., S. Bony, D. Winker, G. Cesana, J. L. Dufresne, P. Minnis, C. J. Stubenrauch, and S. Zeng (2010), The GCM-Oriented CALIPSO Cloud Product (CALIPSO-GOCCP), *J. Geophys. Res.*, **115**, D00H16, doi:10.1029/2009JD012251.
- Chou, C., and J. D. Neelin (2004), Mechanisms of global warming impacts on regional tropical precipitation, *J. Clim.*, **17**(13), 2688–2701.
- Chou, C., J. D. Neelin, C.-A. Chen, and J.-Y. Tu (2009), Evaluating the “rich-get-richer” mechanism in tropical precipitation change under global warming, *J. Clim.*, **22**(8), 1982–2005.
- Cionni, I., et al. (2011), Ozone database in support of CMIP5 simulations: Results and corresponding radiative forcing, *Atmos. Chem. Phys.*, **11**(21), 11,267–11,292.
- Crueger, T., B. Stevens, and R. Brokopf (2012), The Madden-Julian oscillation in ECHAM6 and the introduction of an objective MJO score, *J. Clim.*, in press.
- Dave, J. V. (1968), Scattering of visible light by large water spheres. *Appl. Opt.*, **8**, 155–164.
- Dee, D. P., et al. (2011), The ERA-Interim reanalysis: configuration and performance of the data assimilation system, *Q. J. R. Meteorol. Soc.*, **137**(656), 553–597.
- Ebert, E. E., and J. A. Curry (1992), A parameterization of ice cloud optical properties for climate models, *J. Geophys. Res.*, **97**(D4), 3831, doi:10.1029/91JD02472.
- Fouquart, Y., and B. Bonnel (1980), Computations of solar heating of the earth's atmosphere—A new parameterization, *Beitr. Phys. Atmos.*, **53**, 35–62.
- Giorgetta, M., E. Manzini, E. Roeckner, M. Esch, and L. Bengtsson (2006), Climatology and forcing of the quasi-biennial oscillation in the MAECHAM5 model, *J. Clim.*, **19**(16), 3882–3901.
- Gregory, J. M., et al. (2004), A new method for diagnosing radiative forcing and climate sensitivity, *Geophys. Res. Lett.*, **31**(3), L03205, doi:10.1029/2003GL018747.
- Hagemann, S. (2002), An improved land surface parameter dataset for global and regional climate models, *Tech. Rep. 336*, Max Planck Institute for Meteorology, Hamburg, Germany.
- Hale, G. M., and M. R. Querry (1973), Optical constants of water in the 200 nm to 200 m wavelength region, *Appl. Opt.*, **12**, 555–563.
- Held, I. M., and B. J. Soden (2006), Robust responses of the hydrological cycle to global warming, *J. Clim.*, **19**(21), 5686–5699.
- Hines, C. O. (1997), Doppler-spread parameterization of gravity-wave momentum deposition in the middle atmosphere. Part 1: Basic formulation, *J. Atmos. Sol. Terr. Phys.*, **59**(4), 371–386.



- Hines, C. O. (2012), Doppler-spread parameterization of gravity-wave momentum deposition in the middle atmosphere. Part 2: Broad and quasi monochromatic spectra, and implementation, *J. Atmos. Sol. Terr. Phys.*, 59(4), 387–400.
- Hurt, G. C., et al. (2011), Harmonization of land-use scenarios for the period 1500–2100: 600 years of global gridded annual land-use transitions, wood harvest, and resulting secondary lands, *Clim. Change*, 109(1–2), 117–161.
- Iacono, M. J., J. S. Delamere, E. J. Mlawer, M. W. Shephard, S. A. Clough, and W. D. Collins (2008), Radiative forcing by long-lived greenhouse gases: Calculations with the AER radiative transfer models, *J. Geophys. Res.*, 113, D13103, doi:10.1029/2008JD009944.
- Jöckel, P., R. von Kuhlmann, M. G. Lawrence, B. Steil, C. A. M. Brenninkmeijer, P. J. Crutzen, P. J. Rasch, and B. Eaton (2001), On a fundamental problem in implementing flux-form advection schemes for tracer transport in 3-dimensional general circulation and chemistry transport models, *Q. J. R. Meteorol. Soc.*, 127(573), 1035–1052.
- Jungclaus, J. H., et al. (2010), Climate and carbon-cycle variability over the last millennium, *Clim. Past*, 6(5), 723–737.
- Kato, S., et al. (2012), Improvement of top-of-atmosphere and surface irradiance computations with CALIPSO, CloudSAT, and MODIS-derived cloud and aerosol properties, *J. Clim.*, 25, 1–63.
- Kidston, J., and E. P. Gerber (2010), Intermodel variability of the poleward shift of the austral jet stream in the CMIP3 integrations linked to biases in 20th century climatology, *Geophys. Res. Lett.*, 37(9), L09708, doi:10.1029/2010GL042873.
- Li, C., J.-S. Storch, and J. Marotzke (2012), Deep-ocean heat uptake and equilibrium climate response, *Clim. Dyn.*, doi:10.1007/s00382-012-1350-z, [Available at: <http://link.springer.com/article/10.1007/s00382-012-1350-z/fulltext.html>].
- Liess, S., L. Bengtsson, and K. Arpe (2004), The intraseasonal oscillation in ECHAM4. Part I: Coupled to a comprehensive ocean model, *Clim. Dyn.*, 22(6), 653–669.
- Lin, S.-J., and R. B. Rood (1996), Multidimensional flux-form semi-Lagrangian transport schemes, *Mon. Weather Rev.*, 124(9), 2046–2070.
- Lohmann, U., and E. Roeckner (1996), Design and performance of a new cloud microphysics scheme developed for the ECHAM general circulation model, *Clim. Dyn.*, 12(8), 557–572.
- Lohmann, U., P. Stier, C. Hoose, S. Ferrachat, E. Roeckner, and J. Zhang (2007), Cloud microphysics and aerosol indirect effects in the global climate model ECHAM5-HAM, *Atmos. Chem. Phys. Discuss.*, 7(2), 3719–3761.
- Lott, F. (1999), Alleviation of stationary biases in a gcm through a mountain drag parameterization scheme and a simple representation of mountain lift forces, *Mon. Weather Rev.*, 127(5), 788–801.
- Louis, J.-F. (1979), A parametric model of vertical eddy fluxes in the atmosphere, *Boundary-Layer Meteorol.*, 17(2), 187–202.
- Lunkeit, F., R. Sausen, and J. M. Oberhuber (1996), Climate simulations with the global coupled atmosphere-ocean model ECHAM2/OPYC. Part I: Present-day climate and ENSO events, *Clim. Dyn.*, 12(3), 195–212.
- Maier-Reimer, E., U. Mikolajewicz, and K. Hasselmann (1993), Mean circulation of the Hamburg LSG OGCM and its sensitivity to the thermohaline surface forcing, *J. Phys. Oceanogr.*, 23(4), 731–757.
- Manzini, E., and L. Bengtsson (1996), Stratospheric climate and variability from a general circulation model and observations, *Clim. Dyn.*, 12(9), 615–639.
- Manzini, E., N. McFarlane, and C. McLandress (1997), Impact of the Doppler spread parameterization on the simulation of the middle atmosphere circulation using the MA/ECHAM4 general circulation model, *J. Geophys. Res.*, 102(D22), 25,751–25,762.
- Manzini, E., M. Giorgetta, M. Esch, L. Kornblüeh, and E. Roeckner (2006), The influence of sea surface temperatures on the northern winter stratosphere: Ensemble simulations with the MAECHAM5 model, *J. Clim.*, 19(16), 3863–3881.
- Marsland, S., H. Haak, J. H. Jungclaus, M. Latif, and F. Röske (2003), The Max-Planck-Institute global ocean/sea ice model with orthogonal curvilinear coordinates, *Ocean Modell.*, 5(2), 91–127.
- Mauritsen, T., et al. (2012), Tuning the climate of a global model, *J. Adv. Model. Earth Syst.*, 4, M00A01, doi:10.1029/2012MS000154.
- Miller, M. J., T. N. Palmer, and R. Swinbank (1989), Parameterization and influence of subgrid-scale orography in general circulation and numerical weather prediction models, *Meteorol. Atmos. Phys.*, 40(1), 84–109.
- Möbis, B. and B. Stevens (2012), Factors controlling the position of the ITCZ on an aquaplanet, *J. Adv. Model. Earth Syst.*, 4, M00A04, doi:10.1029/2012MS000199.
- Nordeng, T. E. (1994), Extended versions of the convective parameterization scheme at ECMWF and their impact on the mean and transient activity of the model in the tropics, *Tech. Rep. 206*, ECMWF, Reading, U. K.
- Palmer, T. N., G. J. Shutts, and R. Swinbank (1986), Alleviation of a systematic westerly bias in general circulation and numerical weather prediction models through an orographic gravity wave drag parameterization, *Q. J. R. Meteorol. Soc.*, 112(474), 1001–1039.
- Pongratz, J., C. Reick, T. Raddatz, and M. Claussen (2008), A reconstruction of global agricultural areas and land cover for the last millennium, *Global Biogeochem. Cycles*, 22(3), GB3018, doi:10.1029/2007GB003153.
- Pozzoli, L., I. Bey, S. Rast, M. G. Schultz, P. Stier, and J. Feichter (2008), Trace gas and aerosol interactions in the fully coupled model of aerosol-chemistry-climate ECHAM5-HAMMOZ: 1. Model description and insights from the spring 2001 TRACE-P experiment, *J. Geophys. Res.*, 113, D07308, doi:10.1029/2007JD009007.
- Raddatz, T., C. Reick, W. Knorr, and J. Kattge (2007), Will the tropical land biosphere dominate the climate-carbon cycle feedback during the twenty-first century? *Clim. Dyn.*, 29(6), 565–574, doi:10.1007/s00382-007-0247-8.
- Ramankutty, N. and J. A. Foley (1999), Estimating historical changes in global land cover: Croplands from 1700 to 1992, *Global Biogeochem. Cycles*, 13(4), 997–1027.
- Randall, D., et al. (2007), Climate models and their evaluation, in *Climate Change 2007: The Physical Science Basis. Contribution of Working Group I to the Fourth Assessment Report of the Intergovernmental Panel on Climate Change*, edited by S. Solomon et al., pp. 1–74, Cambridge Univ. Press, Cambridge, U. K.
- Reichler, T., and J. Kim (2008), How well do coupled models simulate today's climate? *Bull. Am. Meteorol. Soc.*, 89(3), 303–311.
- Roeckner, E., L. Dümenil, E. Kirk, F. Lunkeit, M. Ponater, B. Rockel, R. Sausen, and U. Schlese (1989), The Hamburg version of the ECMWF model (ECHAM), *Tech. Rep. 13*, World Meteorol. Org., Geneva, Switzerland.
- Roeckner, E., et al. (1992), *Simulation of the present-day climate with the ECHAM model: Impact of model physics and resolution*, *Tech. Rep. 93*, Max-Planck-Institut für Meteorologie, Hamburg, Germany.
- Roeckner, E., et al. (1996), The atmospheric general circulation model ECHAM-4: Model description and simulation of present-day climate, *Tech. Rep. 218*, Max-Planck-Institut für Meteorologie, Hamburg, Germany.
- Roeckner, E., et al. (2003), *The atmospheric general circulation model ECHAM5—Part I: Model description*, *Tech. Rep. 349*, Max-Planck-Institut für Meteorologie, Hamburg, Germany.
- Roeckner, E., T. Mauritsen, M. Esch, and R. Brokopf (2012), Impact of melt ponds on Arctic sea ice in past and future climates as simulated by MPI-ESM, *J. Adv. Model. Earth Syst.*, 4, M00A02, doi:10.1029/2012MS000157.
- Rosow, W. and R. Schiffer (1999), Advances in understanding clouds from ISCCP, *Bull. Am. Meteorol. Soc.*, 80(11), 2261–2287.
- Schmidt, H., et al. (2006), The HAMMONIA chemistry climate model: Sensitivity of the mesopause region to the 11-year solar cycle and CO<sub>2</sub> doubling, *J. Clim.*, 19(16), 3903–3931.
- Simmons, A. J., and D. M. Burridge (1981), An energy and angular-momentum conserving vertical finite-difference scheme and hybrid vertical coordinates, *Mon. Weather Rev.*, 109(4), 758–766.
- Simmons, A. J., and J. Chen (1991), The calculation of geopotential and the pressure gradient in the ECMWF atmospheric model: Influence on the simulation of the polar atmosphere and on temperature analyses, *Q. J. R. Meteorol. Soc.*, 117(497), 29–58.
- Simmons, A. J., D. M. Burridge, M. Jarraud, C. Girard, and W. Wergen (1989), The ECMWF medium-range prediction models development of the numerical formulations and the impact of increased resolution, *Meteorol. Atmos. Phys.*, 40(1), 28–60.
- Sperber, K. R., S. Gualdi, S. Legutke, and V. Gayler (2005), The Madden-Julian oscillation in ECHAM4 coupled and uncoupled general circulation models, *Clim. Dyn.*, 25(2–3), 117–140.



- Stenchikov, G. L., I. Kirchner, A. Robock, H.-F. Graf, J. C. Antuña, R. G. Grainger, A. Lambert, and L. Thomason (1998), Radiative forcing from the 1991 Mount Pinatubo volcanic eruption, *J. Geophys. Res.*, *103*, 13,837–13,858.
- Stephens, G. L., et al. (2012), An update on Earth's energy balance in light of the latest global observations, *Nat. Geosci.*, *5*, 691–696, doi:10.1038/ngeo1580.
- Stevens, B., and G. Feingold (2009), Untangling aerosol effects on clouds and precipitation in a buffered system, *Nature*, *461*(7264), 607–613.
- Stevens, B., and S. E. Schwartz (2012), Observing and modeling Earth's energy flows, *Surv. Geophys.*, *33*, 779–816.
- Stier, P., et al. (2005), The aerosol climate model ECHAM5-HAM, *Atmos. Chem. Phys.*, *5*, 1125–1156.
- Sundqvist, H., E. Berge, and J. E. Kristjánsson (1989), Condensation and cloud parameterization studies with a mesoscale numerical weather prediction model, *Mon. Weather Rev.*, *117*(8), 1641–1657.
- Taylor, K. (2001), Summarizing multiple aspects of model performance in a single diagram, *J. Geophys. Res.*, *106*(D7), 7183–7192.
- Taylor, K. E., R. J. Stouffer, and G. A. Meehl (2012), An overview of CMIP5 and the experiment design, *Bull. Am. Meteorol. Soc.*, *93*(4), 485–498.
- Tiedtke, M. (1989), A comprehensive mass flux scheme for cumulus parameterization in large-scale models, *Mon. Weather Rev.*, *117*(8), 1779–1800.
- Timmreck, C. (2001), Three-dimensional simulation of stratospheric background aerosol—First results of a multiannual general circulation model simulation, *J. Geophys. Res.*, *106*, 28.
- Tompkins, A. M. (2002), A prognostic parameterization for the subgrid-scale variability of water vapor and clouds in large-scale models and its use to diagnose cloud cover, *J. Atmos. Sci.*, *59*(12), 1917–1942.
- Trenberth, K. E., and J. T. Fasullo (2010), Simulation of present-day and twenty-first-century energy budgets of the southern oceans, *J. Clim.*, *23*(2), 440–454.
- Waliser, D., et al. (2009), MJO simulation diagnostics, *J. Clim.*, *22*(11), 3006–3030.
- Warren, S. G., and R. E. Brandt (2008), Optical constants of ice from the ultraviolet to the microwave: A revised compilation, *J. Geophys. Res.*, *113*(D14), D14220, doi: 10.1029/2007JD009744.
- Winker, D. M., et al. (2010), The Calipso Mission: A global 3D view of aerosols and clouds, *Bull. Am. Meteorol. Soc.*, *91*(9), 1211–1229.
- Wyant, M. C., C. S. Bretherton, P. N. Blossey, and M. Khairoutdinov (2012), Fast cloud adjustment to increasing CO<sub>2</sub> in a superparameterized climate model, *J. Adv. Model. Earth Syst.*, *4*, M05001, doi:10.1029/2011MS000092.
- Xie, P., and P. A. Arkin (1997), Global precipitation: A 17-year monthly analysis based on gauge observations, satellite estimates, and numerical model outputs, *Bull. Am. Meteorol. Soc.*, *78*(11), 2539–2558.
- Xu, K.-M., and S. K. Krueger (1991), Evaluation of cloudiness parameterizations using a cumulus ensemble model, *Mon. Weather Rev.*, *119*(2), 342–367.
- Zhang, M. H., et al. (2005), Comparing clouds and their seasonal variations in 10 atmospheric general circulation models with satellite measurements, *J. Geophys. Res.*, *110*, D15S02, doi:10.1029/2004JD005021.

---

Corresponding author: B. Stevens, Max Planck Institut für Meteorologie, Bundesstraße 53, KlimaCampus, D-20146 Hamburg, Germany (bjorn.stevens@mpimet.mpg.de)